

# Black Hole Properties of Type-1 Active Galactic Nuclei in the North Ecliptic Pole Wide Field: I. Mid-infrared Sources with Optical Counterparts\*

DOHYEONG KIM,<sup>1</sup> MYUNGSHIN IM,<sup>2</sup> HYUNJIN SHIM,<sup>3</sup> MINJIN KIM,<sup>4,5</sup> GU LIM,<sup>1</sup> JUNYEONG PARK,<sup>1</sup> HAYEONG JEONG,<sup>1</sup>  
YONGJUNG KIM,<sup>6</sup> YONGMIN YOON,<sup>5</sup> SEONG JIN KIM,<sup>7</sup> YOSHIKI TOBA,<sup>8,9</sup> TOMOTSUGU GOTO,<sup>7</sup> NAGISA OI,<sup>10</sup> AND  
HYUNMI SONG<sup>11</sup>

<sup>1</sup>Department of Earth Sciences, Pusan National University, Busan 46241, Republic of Korea

<sup>2</sup>SNU Astronomy Research Center (SNUARC), Astronomy Program, Dept. of Physics & Astronomy, Seoul National University, Seoul 08826, Republic of Korea

<sup>3</sup>Department of Earth Science Education, Kyungpook National University, 80 Daehak-ro, Buk-gu, Daegu 41566, Republic of Korea

<sup>4</sup>Department of Astronomy, Yonsei University, 50 Yonsei-ro, Seodaemun-gu, Seoul 03722, Republic of Korea

<sup>5</sup>Department of Astronomy and Atmospheric Sciences, College of Natural Sciences, Kyungpook National University, Daegu 41566, Republic of Korea

<sup>6</sup>School of Liberal Studies, Sejong University, 209 Neungdong-ro, Gwangjin-Gu, Seoul 05006, Republic of Korea

<sup>7</sup>Institute of Astronomy, National Tsing Hua University, 101, Section 2, Kuang-Fu Road, Hsinchu 30013, Taiwan

<sup>8</sup>Department of Physical Sciences, Ritsumeikan University, 1-1-1 Noji-higashi, Kusatsu, Shiga 525-8577, Japan

<sup>9</sup>Academia Sinica Institute of Astronomy and Astrophysics, 11F of Astronomy-Mathematics Building, AS/NTU, No.1, Section 4, Roosevelt Road, Taipei 10617, Taiwan

<sup>10</sup>Space Information Center, Hokkaido Information University, Nishi-Nopporo 59-2, Ebetsu, Hokkaido 069-8585, Japan

<sup>11</sup>Department of Astronomy and Space Science, Chungnam National University, 99 Daehak-ro, Yuseong-gu, Daejeon 34134, Republic of Korea

## ABSTRACT

We present measurements of black hole (BH) properties of 861 Type-1 active galactic nuclei (AGNs) in the North Ecliptic Pole (NEP)-Wide field. These AGNs are detected in both optical and mid-infrared (MIR) surveys and are identified as Type-1 AGNs in optical spectroscopic surveys. By performing spectral energy distribution (SED) and line fitting, we obtained their MIR continuum luminosities ( $L_{\text{MIR}}$ ) as well as full width at half maximum (FWHM) values for the C IV, Mg II, H $\beta$ , and H $\alpha$  lines. Using these measurements, we derived bolometric luminosities ( $10^{43.20}$ – $10^{47.27}$  erg s<sup>-1</sup>), BH masses ( $10^{7.29}$ – $10^{9.67}$   $M_{\odot}$ ), and Eddington ratios ( $10^{-2.74}$ – $10^{-0.08}$ ) for  $\sim 450$  objects over a wide redshift range ( $z = 0.09$ – $4.71$ ). The use of  $L_{\text{MIR}}$  and FWHM values effectively alleviates the effects of dust extinction, enabling reliable estimates of BH properties even for dust-obscured AGNs. Moreover, we find that 34% of the Type-1 AGNs in the NEP-Wide field are dust-obscured, and that their bolometric luminosities can be significantly underestimated without proper dust extinction correction. Our relatively extinction-free BH property estimates can (i) be combined with multi-wavelength data in the NEP-Wide field to facilitate diverse studies of AGN environments, number densities, host galaxies, and related topics, and (ii) serve as fiducial estimates for SPHEREx and other upcoming infrared (IR) spectroscopic missions covering the NEP-Wide field.

*Keywords:* Quasars (1319) — Active galactic nuclei (16) — Supermassive black holes (1663) — Spectroscopy (1558) — Surveys (1671)

## 1. INTRODUCTION

After the launch of the *AKARI* (Murakami et al. 2007) IR space telescope in February 2006, a targeted survey of the NEP (R.A. = 18<sup>h</sup>00<sup>m</sup>00<sup>s</sup>, Dec.

= +66°33'88'') was carried out. The NEP field was strategically selected owing to its high visibility from *AKARI*'s polar Sun-synchronous orbit, making it optimal for repeated observations. The *AKARI* NEP survey (Matsuhara et al. 2006) consists of two complementary programs – NEP-Deep and NEP-Wide – conducted with InfraRed Camera (IRC; Onaka et al. 2007) using infrared filter sets from 2  $\mu\text{m}$  to 24  $\mu\text{m}$ . Of these, the

\* myungshin.im@gmail.com (MI); shim.hyunjin@gmail.com (HS)

NEP-Wide survey covers an area of  $5.4 \text{ deg}^2$ , with exposure times ranging from 90 to 150 seconds (Lee et al. 2009; Kim et al. 2012).

The *AKARI* NEP-Wide survey is notably complemented by extensive multi-wavelength photometric data from various ground-based observations. Optical photometric data (Hwang et al. 2007; Jeon et al. 2010) were provided by MegaCam on the Canada-France-Hawaii Telescope (CFHT) and by the Seoul National University Camera (SNUCAM; Im et al. 2010) at Maidanak Observatory. More recently, deeper and more comprehensive optical photometry (Oi et al. 2021) covering the entire NEP-Wide field was obtained using the Hyper Suprime-Cam (HSC; Miyazaki et al. 2018) on the Subaru Telescope. Additionally, near-infrared (NIR) *J*- and *H*-band photometric data (Jeon et al. 2014) were acquired with FLAMINGOS at the Kitt Peak National Observatory (KPNO), and  $850 \mu\text{m}$  sub-mm observations (Shim et al. 2020) were conducted using the Submillimetre Common-User Bolometric Array 2 (SCUBA-2) on the James Clerk Maxwell Telescope (JCMT). Furthermore, the NEP-Wide field was also observed at 20 cm (White et al. 2010) over an area of  $1.7 \text{ deg}^2$  using the Westerbork Synthesis Radio Telescope (WSRT).

Given its role as a preferred deep-field region for astronomical satellites, the NEP-Wide field has been extensively observed, both photometrically and spectroscopically, by various space telescopes such as SPHEREx (Doré et al. 2016, 2018), *Euclid* (Euclid Collaboration et al. 2022, 2025), eROSITA (Merloni et al. 2012; Predehl et al. 2021), *ROSAT* (Truemper 1982; Henry et al. 2006), *GALEX* (Martin et al. 2005; Burgarella et al. 2019), *Herschel* (Pilbratt et al. 2010; Burgarella et al. 2019; Pearson et al. 2019), WISE (Wright et al. 2010; Jarrett et al. 2011), and *Spitzer* (Werner et al. 2004; Jarrett et al. 2011; Nayyeri et al. 2018). It is worth noting that, among these missions, SPHEREx is uniquely positioned to provide IR spectroscopic data for all objects in the NEP-Wide field, offering new insights that cannot be derived from photometric observations alone.

Although the NEP-Wide field is well-covered with various photometric and spectroscopic surveys from X-ray to radio, optical spectroscopic observations remain relatively sparse. Shim et al. (2013) provided optical spectra of 1796 objects selected in the NEP-Wide field, which were obtained with Hectospec on the MMT (Fabricant et al. 2008) and Hydra on the WIYN telescope at KPNO (Barden et al. 1994). Using these spectra, they identified 1128 galaxies, 198 type-1 AGNs, and 121 stars. Furthermore, the Dark Energy Spectroscopic Instrument (DESI; DESI Collaboration et al. 2016a,b) collaboration recently released Data Release 1 (DR1; DESI Collabora-

tion et al. 2025) data, which fully covers the NEP-Wide field. The DESI DR1 data include optical spectra for 18 million objects, among which 13 million are classified as galaxies, 1.6 million as quasars, and 4 million as stars.

AGNs are generally classified into Type-1 and Type-2 based on their spectroscopic properties. In the AGN unification model (Urry & Padovani 1995), this classification primarily reflects the orientation of the dust torus surrounding the central SMBH and its accretion disk relative to the observer's line of sight. Type-1 AGNs show both broad and narrow emission lines (BELs and NELs), whereas Type-2 AGNs exhibit only NELs due to obscuration of the region emitting BELs by the dust torus. Beyond the orientation-based dichotomy, there exists another population of dust-obscured AGNs, which are thought to be affected by dust extinction originating in their host galaxies rather than in the dust torus (e.g., Mezcua et al. 2016). They exhibit BELs similar to those of Type-1 AGNs but have very large Balmer decrements, or exhibit only NELs at short wavelengths like Type-2 AGNs while exhibiting BELs at longer wavelengths.

To understand fundamental properties of AGNs, optical spectroscopic data are required. In particular, BH masses (hereafter,  $M_{\text{BH}}$ ) can be measured from optical spectroscopy, using the velocity widths of BELs and the sizes of broad-line regions (BLRs). The velocity widths of BELs are commonly expressed as the full width at half maxima (FWHMs) of the lines. While the sizes of the BLRs can be directly measured using the reverberation mapping method (Peterson et al. 2004), this method is observationally intensive and time-consuming. Hence, the BLR sizes are more commonly measured from single-epoch spectra, using empirical relations between UV or optical continuum luminosities and the BLR sizes (e.g., McLure & Dunlop 2004; Kaspi et al. 2005).

However, the optical spectra easily suffer significantly from dust extinction (e.g., Kim & Im 2018, 2025). For a dust-obscured AGN with a color excess of  $E(B-V) = 2$ , the continuum luminosity at  $5100 \text{ \AA}$  (hereafter,  $L_{5100}$ ) decreases by a factor of 500, but the  $P\alpha$  ( $1.87 \mu\text{m}$ ) and  $\text{Br}\alpha$  ( $4.05 \mu\text{m}$ ) lines decrease only by factors of 2.16 and 1.31, respectively. Hence, alternative approaches using IR spectroscopic data have been developed to estimate BH masses of dust-obscured AGNs. For example, Hydrogen Paschen lines (Kim et al. 2010; Landt et al. 2013; La Franca et al. 2015; Ricci et al. 2017; Kim et al. 2022) and Brackett lines (Kim et al. 2015b, 2022) were newly established as BH mass estimators.

Nevertheless, due to the limited availability of IR spectroscopic data compared to optical spectroscopy, applying these Paschen and Brackett line-based BH mass estimators remains challenging. To address this limitation,

Kim et al. (2023) established new BH mass estimators based on  $L_{\text{MIR}}$  in combination with optical spectroscopy. In this approach, optical spectra provide the velocity width of the BELs, while the  $L_{\text{MIR}}$  values serve as proxies for the BLR sizes. These  $L_{\text{MIR}}$  values are derived from multi-wavelength photometry ranging from optical to MIR, and the resulting  $L_{\text{MIR}}$ -based estimators (Kim et al. 2023) are relatively free from dust extinction. However, it is worth noting that the IR luminosity may be affected by contamination from the host galaxy. In particular, the host galaxy contribution can be significant ( $\sim 50\%$ ) in the NIR, somewhat less so but non-negligible ( $\lesssim 20\%$ ) for some AGNs in the MIR (Kim et al. 2023). Nevertheless, these  $L_{\text{MIR}}$ -based estimators have been successfully applied to both unobscured and dust-obscured AGNs through SED fitting that includes host galaxy component (Kim et al. 2024a,b; Kim & Im 2025).

The aim of this work is to present BH properties of Type-1 AGNs in the NEP-Wide field detected in both optical and MIR surveys. This wide wavelength coverage allows us to apply the  $L_{\text{MIR}}$ -based estimators (Kim et al. 2023) to derive reliable BH properties that are less affected by dust extinction. Combining these BH properties with existing multi-wavelength observations in the NEP-Wide field could facilitate future studies exploring how various factors, such as environment and host galaxy morphology, affect the BH properties. Furthermore, with the upcoming IR low-resolution spectroscopic survey by SPHEREx covering the NEP-Wide field, our results may provide fiducial values for understanding how the IR low-resolution spectroscopy affects the measurements of the fundamental BH properties. Throughout this work, we adopt a standard  $\Lambda$ CDM model of  $H_0 = 70 \text{ km s}^{-1} \text{ Mpc}^{-1}$ ,  $\Omega_m = 0.3$ , and  $\Omega_\Lambda = 0.7$ , which is supported by several observational studies (e.g., Im et al. 1997; Planck Collaboration et al. 2016). All magnitudes are given in the AB magnitude system.

## 2. SAMPLE

Our sample is based on the MIR source catalog in the NEP-Wide field (Kim et al. 2021), which was constructed by cross-matching MIR sources (Kim et al. 2012) with a deep optical catalog (Oi et al. 2021). The MIR observations were carried out by the IRC (Onaka et al. 2007) aboard the *AKARI* space telescope, and details of the data reduction, detection, and photometry are provided in Kim et al. (2012). Each source has photometric measurements in nine bands obtained with the IRC/*AKARI*, which provide continuous coverage from  $2 \mu\text{m}$  to  $25 \mu\text{m}$ , including N2, N3, and N4 (NIR); S7,

S9W, and S11 (MIR-S); and L15, L18W, and L24 (MIR-L).

Moreover, the NEP-Wide field was covered by a deep optical survey (Oi et al. 2021) using the HSC (Miyazaki et al. 2018) on the Subaru telescope, with five photometric bands:  $g$ ,  $r$ ,  $i$ ,  $z$ , and  $y$ . This photometric catalog of the HSC survey reaches a  $5\sigma$  depth of  $\sim 28.1$  mag in the  $g$  band, which is  $\sim 2$  mag deeper than previous optical surveys in the NEP-Wide field (e.g., Hwang et al. 2007).

Kim et al. (2021) present 91,861 *AKARI* MIR sources that were cross-matched with the HSC optical catalog using a matching radius of 1.78 arcseconds, of which 95% were matched within 1.5 arcseconds. The matching radius was determined as the  $3\sigma$  value from the positional offset distributions of the matched sources. These matched sources (hereafter, *AKARI*–HSC sources) serve as the parent sample from which our sample of Type-1 AGNs is drawn. Besides the *AKARI*–HSC sources, 43,294 MIR sources were excluded, which were either not matched to any optical sources or were flagged as unreliable matches due to being located near masked edges or affected by saturated pixels. The detailed description of the matching process is provided in Kim et al. (2021). Consequently, the *AKARI*–HSC sources exclude MIR sources that are not detected in the optical survey, which are considered to be either (i) obscured objects or (ii) high- $z$  sources (Toba et al. 2020).

In addition, Kim et al. (2021) matched various photometric catalogs to the *AKARI*–HSC sources, providing a complementary photometric data set. This complementary data set includes optical data from MegaPrime/CFHT (Huang et al. 2020), MegaCam/CFHT (Hwang et al. 2007), and SNUCAM/Maidanak (Jeon et al. 2010); IR data from FLAMINGOS/KPNO (Jeon et al. 2014), IRAC/*Spitzer* (Nayyeri et al. 2018), WISE (Jarrett et al. 2011), PACS/*Herschel* (Pearson et al. 2019), and SPIRE/*Herschel* (Pearson et al. 2017); and sub-mm measurements from SCUBA-2/JCMT (Shim et al. 2020).

We matched the *AKARI*–HSC sources with the Type-1 AGNs identified from two different optical spectroscopic surveys. First, we used the quasars from the DESI DR1 (DESI Collaboration et al. 2025). In the DESI DR1, quasar candidates were selected using three optical bands ( $g$ ,  $r$ , and  $z$ ) and two IR bands (W1 and W2; Chaussidon et al. 2023). These candidates were spectroscopically confirmed as quasars using the DESI pipeline classifier Redrock (Bailey et al. in prep.), the machine-learning algorithm QuasarNet (Busca & Balland 2018), and the Mg II post-processing pipeline, which further improves quasar classification and redshift estimation

(Chaussidon et al. 2023; Alexander et al. 2023). Note that the DESI quasar selection is optimized for point-like sources and is effectively limited to  $16.5 \text{ mag} \lesssim r \lesssim 23 \text{ mag}$  (Chaussidon et al. 2023). Therefore, this sample may miss Type-1 AGNs that are brighter than the bright limit ( $r \lesssim 16.5 \text{ mag}$ ), fainter than the faint limit ( $r \gtrsim 23 \text{ mag}$ ), or whose photometry is significantly contaminated by host galaxy light.

We matched the DESI DR1 catalog to the *AKARI*–HSC sources using a matching radius of 2.2 arcseconds, which corresponds to twice the seeing size in the  $z$  band of the DESI Legacy Imaging Survey (Dey et al. 2019). This yields 14,797 matched sources, of which 832 are classified as DESI quasars. Note that the false-match rate is expected to be  $\sim 2.2\%$ . To estimate the false-match rate, we performed a control test by randomly shifting the DESI quasar positions by 10 arcseconds and repeating the cross-matching with the *AKARI*–HSC sources using the same 2.2 arcsecond radius. In total, 831 DESI DR1 quasars were cross-matched with the *AKARI*–HSC sources. Note that, among the 831 DESI DR1 quasars, one object was matched with two *AKARI*–HSC sources, and the nearest *AKARI*–HSC source was adopted as the counterpart.

Second, we used the Type-1 AGNs identified by Shim et al. (2013), who selected Type-1 AGN candidates based on two IR color criteria,  $N2 - N4 > 0$  and  $S7 - S11 > 0$ . Using Hectospec on the MMT and Hydra on the WIYN, they obtained optical spectra of the AGN candidates with  $R$ -band magnitudes brighter than 22.5, among which 198 were identified as Type-1 AGNs. Among them, we found 163 Type-1 AGNs that were matched to the *AKARI*–HSC sources. However, since 133 of them were already identified as DESI quasars, we used only the remaining 30 objects as Type-1 AGNs from Shim et al. (2013).

In conclusion, a total of 861 *AKARI*–HSC sources were identified as Type-1 AGNs, which were used as the main sample in this study. In this paper, the term “AGN” encompasses both luminous quasars and lower-luminosity AGNs. Figure 1 presents the distributions of  $W1$ -band magnitudes and redshifts for our sample, which are not significantly different from those of Sloan Digital Sky Survey (SDSS) Data Release 14 (DR14) quasars (Pâris et al. 2018; Rakshit et al. 2020). Our sample spans a wide range of redshifts ( $0.09 < z < 4.71$ ), BH mass ( $10^{7.29} < M_{\text{BH}}/M_{\odot} < 10^{9.67}$ ), and bolometric luminosity (hereafter,  $L_{\text{bol}}$ ;  $10^{43.20} < L_{\text{bol}}/\text{erg s}^{-1} < 10^{47.27}$ ). Note that these values were estimated using the  $L_{\text{MIR}}$ -based estimators, as described in Sections 4.1 and 4.2.

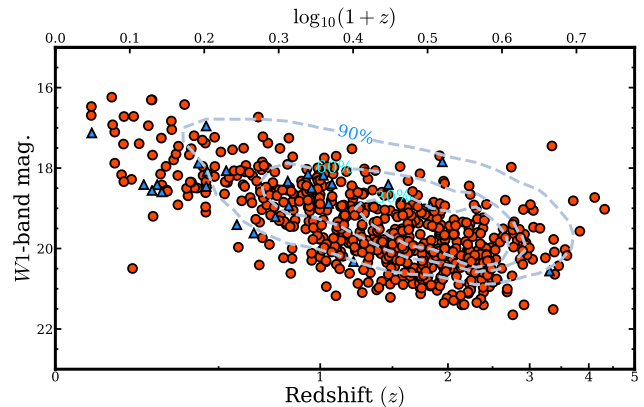


**Figure 1.** Redshift versus  $W1$ -band magnitude. Red circles and blue triangles represent the 861 Type-1 AGNs used in this study, identified from DESI DR1 and Shim et al. (2013), respectively. The gray dashed contours present the distribution of redshifts and  $W1$ -band magnitudes of SDSS DR14 quasars for comparison.

### 3. ANALYSIS

#### 3.1. SED fitting

In order to estimate  $L_{\text{bol}}$  and  $M_{\text{BH}}$  using the  $L_{\text{MIR}}$ -based estimators (Kim et al. 2023), measurements of the monochromatic continuum luminosities,  $\lambda L_{\lambda}$ , at rest-frame  $3.4 \mu\text{m}$  and  $4.6 \mu\text{m}$  (hereafter,  $L_{3.4}$  and  $L_{4.6}$ , respectively) are required. To obtain the  $L_{3.4}$  and  $L_{4.6}$  values for our sample, we performed SED fitting using multi-wavelength photometry ranging from optical to MIR.

For the SED fitting, we used the photometric data from the HSC/Subaru ( $g$ ,  $r$ ,  $i$ ,  $z$ , and  $y$  bands; Oi et al. 2021), the FLAMINGOS/KPNO ( $J$  and  $H$  bands; Jeon et al. 2014), the IRC/*AKARI* ( $N2$ ,  $N3$ ,  $N4$ ,  $S7$ ,  $S9W$ ,  $S11$ ,  $L15$ ,  $L18W$ , and  $L24$  bands; Kim et al. 2012), the WISE ( $W1$ ,  $W2$ , and  $W3$  bands; Jarrett et al. 2011), and the IRAC/*Spitzer* ( $IRAC1$ ,  $IRAC2$ ,  $IRAC3$ , and  $IRAC4$  bands; Nayyeri et al. 2018). These photometric data, originally obtained from the multiple surveys, were cross-matched and assembled into a unified catalog by Kim et al. (2021), from which we adopted the photometry for our analysis. An intrinsic fluctuation of  $\sigma_m = 0.035 \text{ mag}$  (Kim et al. 2015b), arising from AGN variability, was added in quadrature to the original photometric uncertainties in each band. In addition, only photometric data with signal-to-noise ratios (S/N) greater than 3 were included in the SED fitting. Note that the WISE  $W4$  photometry was excluded from the SED fitting owing to its photometric calibration issues (Brown et al. 2014).

**Table 1.** Basic Properties and Measurements of Type-1 AGNs in the NEP-Wide Field

AKARI ID	Spec. ID <sup>a</sup>	$\alpha_{J2000}$	$\delta_{J2000}$	redshift	$\log\left(\frac{L_{3.4}}{\text{erg s}^{-1}}\right)^b$	$\log\left(\frac{L_{4.6}}{\text{erg s}^{-1}}\right)^b$	$E(B-V)$	FWHM					
								(deg.)	(deg.)	(z)	(mag.)	C IV ( $\text{km s}^{-1}$ )	Mg II ( $\text{km s}^{-1}$ )
133109	39633470514793582	269.5586	67.7215	0.205	43.82 ± 0.02	43.81 ± 0.02	0.00	–	–	3760 ± 120	2840 ± 30	–	–
135036	39633461161495358	272.9552	66.7585	0.996	44.71 ± 0.02	44.69 ± 0.02	0.00	–	3840 ± 710	–	–	–	–
44872	39633456321267046	272.0693	66.1369	0.293	–	–	0.00	–	–	–	–	5290 ± 200	–
134539	39633463535471858	272.0972	67.0477	0.250	–	–	–	–	–	–	–	9360 ± 1020	–
133581	39633465880087464	270.4529	67.3362	0.333	43.81 ± 0.02	43.79 ± 0.02	0.00	–	–	3150 ± 120	2750 ± 60	–	–
46186	2305843019946926614	269.2281	65.9080	0.509	44.18 ± 0.02	44.16 ± 0.02	0.00	–	–	–	–	–	–
133141	39633448859602050	269.6010	65.5188	0.326	44.10 ± 0.02	44.08 ± 0.02	0.00	–	3200 ± 290	3990 ± 180	3740 ± 290	–	–
132335	39633448851210769	267.9706	65.4902	0.401	–	–	–	–	–	–	–	–	–
132310	39633451355212011	267.9039	65.6752	0.825	45.02 ± 0.02	45.00 ± 0.02	0.22	–	3260 ± 220	3610 ± 120	–	–	–
132768	39633453842434564	268.8884	66.116	0.198	–	–	0.00	–	–	–	–	–	–
133094	39633453846628993	269.5275	66.0083	0.087	–	–	–	–	–	–	–	5560 ± 220	–
133299	39633453850822123	269.910	65.9765	2.235	45.57 ± 0.03	45.55 ± 0.03	0.00	–	–	–	–	–	–
132336	39633453838238503	267.9721	65.9240	0.307	–	–	0.00	–	–	–	–	–	–
53113	39633453838239265	268.0851	65.9499	0.348	–	–	–	–	–	–	–	–	–
132128	39633456287715657	267.5017	66.2005	0.524	–	–	–	–	6050 ± 1200	–	–	–	–
132658	39633458728797750	268.6906	66.3971	0.088	–	–	–	–	–	4870 ± 500	2930 ± 40	–	–
132883	39633458732990946	269.1327	66.4189	0.263	43.59 ± 0.02	43.57 ± 0.02	0.28	–	–	–	–	–	–

<sup>a</sup> Spectroscopic ID adopted from DESI DR1 and Shim et al. (2013).

<sup>b</sup> Extinction-corrected  $L_{\text{MIR}}$  values.

NOTE—Columns (1)–(2): AKARI and spectroscopic ID. Columns (3)–(4): Right Ascension and Declination in degrees. Column (5): Redshift. Columns (6)–(7):  $L_{\text{MIR}}$  values. Column (8): Dust extinction  $E(B-V)$ . Columns (9)–(12): FWHMs of emission lines. This table is fully available in a machine-readable format.

The SED fitting was performed following the methodology described in Kim et al. (2023). The photometric flux density,  $f(\lambda)$ , is fitted with a sum of reddened spectra:

$$f(\lambda) = C_1 A(\lambda) + C_2 E(\lambda) + C_3 S(\lambda) + C_4 I(\lambda), \quad (1)$$

where  $A(\lambda)$ ,  $E(\lambda)$ ,  $S(\lambda)$ , and  $I(\lambda)$  represent reddened AGN, elliptical, spiral, and irregular galaxy spectra, respectively, with each component scaled by its corresponding coefficient, denoted  $C_1$  through  $C_4$ . These reddened AGN and galaxy spectra are derived from the intrinsic spectral templates  $A_0(\lambda)$ ,  $E_0(\lambda)$ ,  $S_0(\lambda)$ , and  $I_0(\lambda)$ . The intrinsic AGN template is adopted from Krawczyk et al. (2013), whereas the galaxy templates are taken from Assef et al. (2010). While several alternative AGN templates are available (e.g., Richards et al. 2006; Assef et al. 2010), they introduce no significant difference in the SED fitting results (Kim et al. 2023, 2024b; Kim & Im 2025).

For the SED fitting, we used the  $f(\lambda)$  that had already been corrected for Galactic extinction. The extinction corrections for each band were adopted from Oi et al. (2021), based on a reddening value of  $E(B-V) = 0.046$  for the NEP-Wide field (Schlegel et al. 1998). In addition, intrinsic extinction (i.e., dust obscuration within the host galaxy) was applied to the spectral templates to obtain the reddened spectra. To account for dust extinction, we adopted the reddening law of Cardelli et al. (1989), assuming  $R_V = 3.1$  (e.g., Weingartner & Draine

2001). Since this law is significantly different from other reddening laws (e.g., Calzetti et al. 2000) in the UV due to the 2175 Å bump, we excluded the  $f(\lambda)$  values at wavelengths shorter than 3000 Å from the SED fitting.

Note that the NEP-Wide field covers a large area, while the spatial variations in the reddening values are small. The measured  $E(B-V)$  values in this field (Schlegel et al. 1998) range from 0.044 to 0.047. Moreover, the reddening value can be estimated differently depending on the attenuation curve or adopted SED model (e.g., Galametz et al. 2017). For instance, Schlafly & Finkbeiner (2011) reported  $E(B-V) = 0.040$  for the NEP-Wide field. However, such differences have a negligible effect on the SED fitting, producing an extinction-corrected magnitude difference of only  $\sim 0.03$  mag even at 3000 Å, which is the shortest fitting wavelength used in the SED fitting.

We used the MPFIT (Markwardt 2009) procedure in IDL for the SED fitting, and representative examples of the fitting results are shown in Figure 2. From the SED fitting, we obtained the  $L_{3.4}$ ,  $L_{4.6}$ , and  $E(B-V)$  values with their uncertainties for our sample, and these uncertainties are the formal errors derived from the fitting routine based on the input flux uncertainties. Note that we performed the SED fitting only when the number of photometric data exceeded five.

However, we only used these estimates if the following criteria were met. For the  $L_{3.4}$ , the AGN fraction at 3.4  $\mu\text{m}$  had to be greater than 0.5 (i.e.,  $C_1 A(3.4 \mu\text{m}) >$

$\frac{1}{2}f(3.4\ \mu\text{m})$  in Equation 1), and the SED fitting had to include at least one photometric data point at rest-frame wavelength longer than  $3.4\ \mu\text{m}$ . Similarly, the  $L_{4.6}$  values required an AGN fraction greater than 0.5 at  $4.6\ \mu\text{m}$ , and at least one photometric data point beyond  $4.6\ \mu\text{m}$  in the SED fitting. Note that, when the AGN fraction is low, the MIR SED can be dominated by the host galaxy, which may compromise the reliability of the  $L_{\text{MIR}}$  measurement. Moreover, in both cases, we required at least one photometric data point at rest-frame wavelengths shorter than  $0.8\ \mu\text{m}$ , since reliable  $E(B - V)$  estimates cannot be obtained in the absence of short-wavelength data. At  $z \gtrsim 2.4$ , this becomes challenging because the HSC photometric bands correspond to rest-frame wavelengths below  $0.3\ \mu\text{m}$  and were thus excluded from the SED fitting, while the relatively shallow NIR photometry often fails to provide sufficient S/N data points.

Finally, using the reliable  $L_{3.4}$ ,  $L_{4.6}$ , and  $E(B - V)$  values, we obtained extinction-corrected  $L_{3.4}$  and  $L_{4.6}$  values for 609 and 532 objects, respectively. These extinction-corrected luminosities are listed in Table 1. Note that the  $E(B - V)$  estimates could be affected by various intrinsic AGN continuum slopes, but the effects of such continuum slope variations on the  $L_{\text{MIR}}$  measurements are not significant (Kim et al. 2024d).

### 3.2. Line fitting

In order to estimate  $M_{\text{BH}}$  using the  $L_{\text{MIR}}$ -based estimators (Kim et al. 2023), we fitted the  $\text{H}\alpha$ ,  $\text{H}\beta$ ,  $\text{Mg II}$ , and  $\text{C IV}$  lines to obtain the FWHMs of their BEL components. For this line fitting, we used the optical spectra from DESI DR1 (DESI Collaboration et al. 2025) and Shim et al. (2013) after applying Galactic extinction corrections as described in Section 3.1. Note that the DESI spectra cover wavelengths from 3600 to 9800 Å. Shim et al. (2013) provide spectroscopic data obtained with Hectospec/MMT and Hydra/WIYN, which cover 3700–8500 Å and 4500–9000 Å, respectively. The wavelength ranges of these datasets are broadly comparable.

To fit these lines, we used the PyQSOFit code (Guo et al. 2018; Shen et al. 2019) in Python. For each line, the fitting was performed separately using the spectral region within  $\pm 1000\ \text{Å}$  of the line center. During the fitting process, the spectra were simultaneously decomposed into continuum and emission-line components, with the continuum modeled as a combination of a single power-law and an empirical Fe II emission template (Shen et al. 2019). Note that host galaxy subtraction was not performed during the continuum fitting. However, since the continuum fitting was restricted to a relatively narrow wavelength range, the host galaxy contribution was effectively incorporated into the power-law

model, and the FWHM measurements of the BELs are not significantly affected.

After subtracting the continuum component, we simultaneously fitted the emission line components, which consist of multiple line complexes. The  $\text{Mg II}$  complex includes both broad and narrow  $\text{Mg II}$  lines. The  $\text{H}\beta$  complex comprises broad and narrow  $\text{H}\beta$  lines, as well as the  $[\text{O III}] \lambda\lambda 4959, 5007$  doublet (including core and wing components). The  $\text{H}\alpha$  complex includes broad and narrow  $\text{H}\alpha$  lines, along with the  $[\text{N II}] \lambda\lambda 6549, 6585$  and  $[\text{S II}] \lambda\lambda 6718, 6732$  doublets. In contrast, the  $\text{C IV}$  line is modeled with only a broad line, as it does not form a line complex. Note that the  $[\text{O III}]$  line often exhibits a wing component (e.g., Singha et al. 2022), which is commonly interpreted as evidence of gas outflows. A single Gaussian (representing only the core component) fit to the  $[\text{O III}]$  profile can therefore yield unreliable estimates of the line width and velocity offset, and we find that the  $\text{H}\beta$  FWHM estimate can differ by  $\sim 3.5\%$  when the  $[\text{O III}]$  wing component is omitted.

To fit the broad lines, we used multi-Gaussian models: three Gaussians were used for  $\text{C IV}$ ,  $\text{H}\beta$ , and  $\text{H}\alpha$ , and two for  $\text{Mg II}$ . These Gaussian models follow the fitting scheme adopted by Rakshit et al. (2020). To obtain the FWHM values for the broad lines, we measured the FWHM from the composite profile of the multi-Gaussian model, following widely adopted methods in previous studies (e.g., Rakshit et al. 2020; Shen et al. 2019). Occasionally, an additional, extremely broad and faint Gaussian component was included, but it contributes negligibly to the composite profile and does not affect the derived FWHM value. Note that the uncertainties in the FWHM estimates were derived using a Monte Carlo simulation. Each Gaussian component was randomly varied with its  $1\sigma$  error, and the FWHM was recalculated over 1000 random samples. The standard deviation of the resulting FWHM distribution was adopted as the FWHM uncertainty.

In this fitting, the broad lines were defined as those having FWHM values exceeding  $2000\ \text{km s}^{-1}$ , following Kim et al. (2023, 2024b). Although various criteria for broad lines have been adopted in other studies (e.g., Xu et al. 2007; Suh et al. 2019), this criterion effectively excludes narrow-line Seyfert 1 galaxies (e.g., Zhou et al. 2006). Moreover, the narrow lines were constrained to have FWHM values less than  $1000\ \text{km s}^{-1}$ . For these lines, the core components were required to have velocity offsets within  $\pm 1000\ \text{km s}^{-1}$ , while the wing components were allowed to shift up to  $3000\ \text{km s}^{-1}$  from the line center.

Note that the  $\text{C IV}$  line was not fitted when strong broad absorption features were present, such as broad

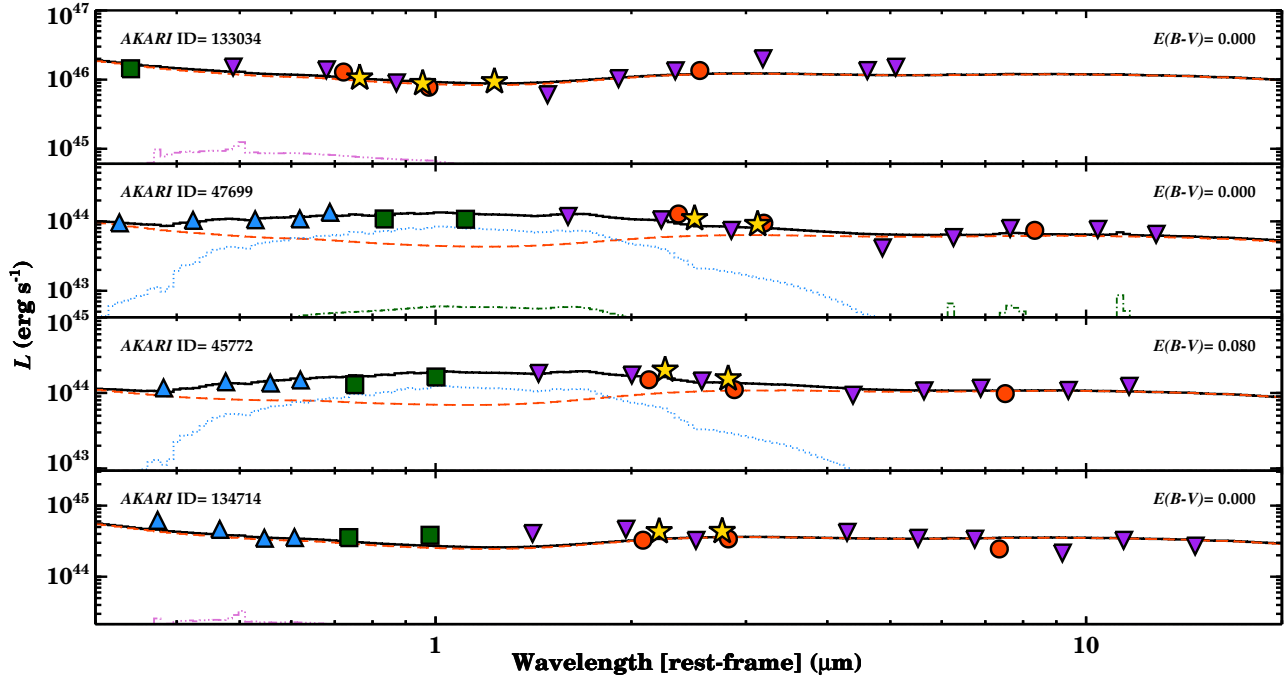


**Figure 2.** Best-fit SED results and corresponding photometric data for four randomly selected Type-1 AGNs. Blue triangles, green squares, purple triangles, red circles, and yellow stars represent the photometric data from HSC/Subaru (Oi et al. 2021), FLAMINGOS/KPNO (Jeon et al. 2014), IRC/AKARI (Kim et al. 2012), WISE (Jarrett et al. 2011), and IRAC/Spitzer (Nayyeri et al. 2018), respectively. The solid black line shows the best-fit SED model, while the dashed red, dotted blue, dot-dashed green, and dot-dot-dashed purple lines represent the reddened spectra of AGN, elliptical, spiral, and irregular galaxies, respectively.

absorption lines (BALs), which are believed to originate from high-velocity outflowing gas. In such cases, both the continuum and the emission-line components were excluded from fitting, since reliable FWHM measurements cannot be obtained. This is because simultaneously modeling asymmetric absorption features and multi-component emission lines is highly uncertain and often leads to non-physical or unstable fitting outcomes.

Figure 3 shows examples of the line fitting results. The FWHM values of the broad  $H\alpha$ ,  $H\beta$ , Mg II, and C IV lines were corrected for the effects of instrumental spectral resolution. This correction was applied using the relation of  $\text{FWHM}^2 = (\text{FWHM}_{\text{fit}})^2 - (\text{FWHM}_{\text{inst}})^2$ , where  $\text{FWHM}_{\text{fit}}$  is the measured FWHM from the fit, and  $\text{FWHM}_{\text{inst}}$  is the instrumental resolution. Note that the instrumental resolution of the DESI spectra corresponds to a spectral resolution of  $1.8 \text{ \AA}$ . For the spectra from Shim et al. (2013), the Hectospec/MMT has a spectral resolution of  $6.2 \text{ \AA}$ , while the Hydra/WYIN provides a resolution of  $5.7 \text{ \AA}$ . We then used only reliable FWHM measurements, selecting those with  $\text{FWHM}/\text{FWHM}_{\text{err}} > 3$ , where  $\text{FWHM}_{\text{err}}$  is the uncertainty from the fit.

For some objects, multiple broad emission lines were available for FWHM measurements. Specifically, 205 objects have both C IV and Mg II FWHM measure-

ments, 47 have both Mg II and  $H\beta$ , and 19 have both  $H\beta$  and  $H\alpha$ . The corresponding rms scatters of the logarithmic FWHM differences are 0.119, 0.100, and 0.105 dex, respectively, which are slightly larger than those reported by Bisogni et al. (2017) (0.070, 0.068, and 0.043 dex), but comparable to the  $\sim 0.1$  dex scatter between the  $H\alpha$  and  $H\beta$  line reported by Greene & Ho (2005). Nevertheless, our rms scatters are smaller than those obtained for SDSS quasars, which show rms scatters of 0.211, 0.129, and 0.131 dex when only objects with  $S/N > 3$  are considered (Rakshit et al. 2020). The larger C IV-Mg II scatter in Rakshit et al. (2020) is plausibly due to the inclusion of outflow-affected C IV lines, whereas such outflow-affected lines were excluded from our line fitting.

In total, we obtained reliable FWHM measurements for 585 objects: 326 for C IV, 420 for Mg II, 68 for  $H\beta$ , and 43 for  $H\alpha$ . The redshift coverage for each line is  $z = 1.42\text{--}4.32$  for C IV,  $0.32\text{--}2.39$  for Mg II,  $0.09\text{--}0.98$  for  $H\beta$ , and  $0.09\text{--}0.46$  for  $H\alpha$ . Overall, the sample spans  $0.09 \leq z \leq 4.32$ , and most objects ( $\sim 80\%$ ) are located within  $0.5 \leq z \leq 2.5$ . These measurements are summarized in Table 1.

## 4. RESULT

### 4.1. Bolometric luminosity

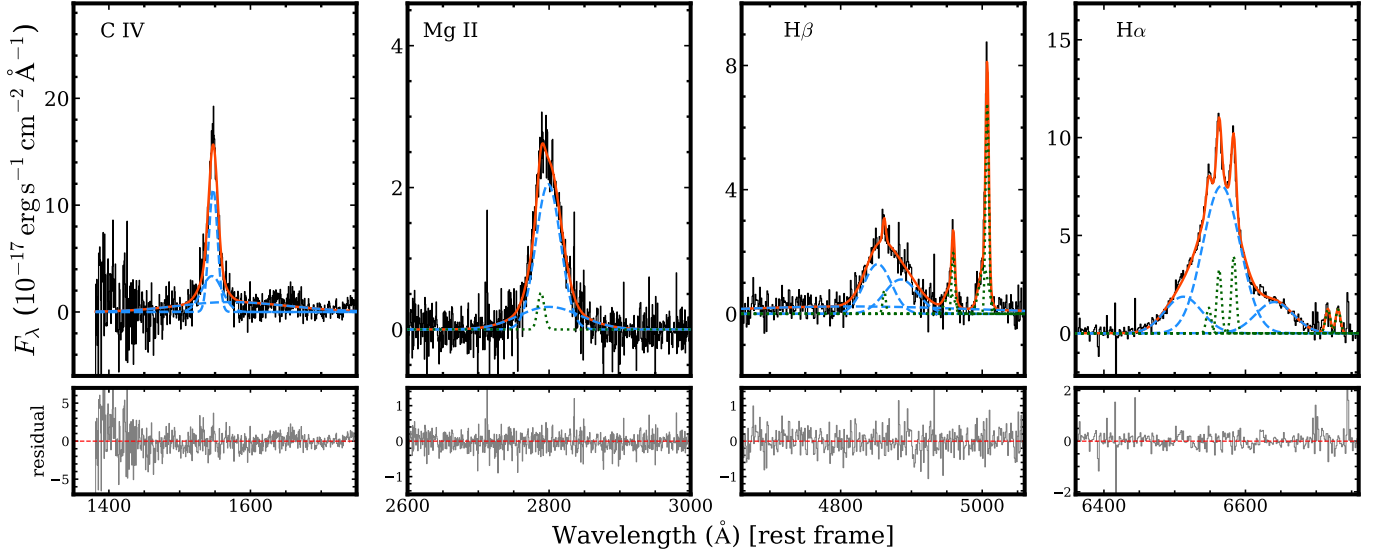


**Figure 3.** Examples of spectral fitting results for the C IV, Mg II, H $\beta$ , and H $\alpha$  line complexes. In the upper panels, the black lines show the rest-frame continuum-subtracted spectra. The dashed blue and dotted green lines represent the broad and narrow emission line models, respectively, and the solid red lines indicate the combined best-fit model of the broad and narrow lines. The lower panels show the fitting residuals.

In this subsection, we derived the bolometric luminosities of our sample using the  $L_{\text{MIR}}$ -based estimators (Kim et al. 2023). For this, we used the extinction-corrected  $L_{3.4}$  and  $L_{4.6}$  values obtained in Section 3.1. The  $L_{\text{MIR}}$ -based  $L_{\text{bol}}$  estimators are

$$\begin{aligned} & \log \left( \frac{L_{\text{bol}}}{10^{44} \text{ erg s}^{-1}} \right) \\ &= (0.722 \pm 0.021) + (0.993 \pm 0.031) \log \left( \frac{L_{3.4}}{10^{44} \text{ erg s}^{-1}} \right) \end{aligned} \quad (2)$$

and

$$\begin{aligned} & \log \left( \frac{L_{\text{bol}}}{10^{44} \text{ erg s}^{-1}} \right) \\ &= (0.739 \pm 0.021) + (0.993 \pm 0.031) \log \left( \frac{L_{4.6}}{10^{44} \text{ erg s}^{-1}} \right), \end{aligned} \quad (3)$$

with an intrinsic scatter of 0.126 dex for both relations. Note that deriving  $L_{\text{bol}}$  from a full SED covering X-ray to IR wavelengths (e.g., Krawczyk et al. 2013) is the most reliable estimate. However, this is not feasible for all sources given the wide redshift range and photometric coverage of our sample. Therefore, we adopted  $L_{\text{MIR}}$  derived from the SED fitting (Kim et al. 2023) as a proxy for  $L_{\text{bol}}$ .

Using these  $L_{\text{MIR}}$ -based estimators, we obtained  $L_{\text{bol}}$  values based on  $L_{3.4}$  and  $L_{4.6}$  for 609 and 532 objects, respectively. Since both  $L_{3.4}$  and  $L_{4.6}$  were derived from the single AGN component obtained through a common SED fit, the resulting  $L_{\text{bol}}$  values are effectively the same. Any difference is negligible in practice com-

pared to the intrinsic scatter of  $\sim 0.13$  dex. Using these measurements, we obtained  $L_{\text{bol}}$  values for 639 objects, each with at least one available measurement of  $L_{3.4}$  or  $L_{4.6}$ . These  $L_{\text{bol}}$  values are listed in Table 2 and span a wide range from  $10^{43.20}$  to  $10^{47.27}$  erg s $^{-1}$ , with mean and median values of  $10^{45.49}$  and  $10^{45.55}$  erg s $^{-1}$ , respectively, and a standard deviation of 0.61 dex. Note that the uncertainties in the  $L_{\text{bol}}$  values were estimated by taking into account both the uncertainties from the  $L_{\text{MIR}}$  measurements and those in the parameters of the  $L_{\text{bol}}$  estimators.

#### 4.2. Black Hole Mass

In this subsection, we estimate the BH masses using the  $L_{\text{MIR}}$ -based estimators. For objects with available FWHM measurements of the H $\beta$  or H $\alpha$  lines, we applied the  $L_{\text{MIR}}$ -based  $M_{\text{BH}}$  estimators presented in Kim et al. (2023). These  $L_{\text{MIR}}$ -based  $M_{\text{BH}}$  estimators can be expressed as

$$\begin{aligned} \log \left( \frac{M_{\text{BH}}}{M_{\odot}} \right) &= \alpha + \beta \log \left( \frac{L_{\text{Cont}}}{10^{44} \text{ erg s}^{-1}} \right) \\ &+ \gamma \log \left( \frac{\text{FWHM}_{\text{Line}}}{10^3 \text{ km s}^{-1}} \right), \end{aligned} \quad (4)$$

where the coefficients  $\alpha$ ,  $\beta$ , and  $\gamma$  are listed in Table 3.

For objects with FWHM measurements of the Mg II and/or C IV lines, we modified the H $\alpha$  line-based  $M_{\text{BH}}$  estimators (i.e., D and H in Table 3) by applying the empirical relations between  $\text{FWHM}_{\text{H}\alpha}$  and FWHMs of

**Table 2.** BH Properties of Type-1 AGNs in the NEP-Wide Field

<i>AKARI</i> ID	$\log\left(\frac{L_{\text{bol}}}{\text{erg s}^{-1}}\right)^a$	$\log\left(\frac{M_{\text{BH}}}{M_{\odot}}\right)^a$	$\log(\lambda_{\text{Edd}})$
133109	44.55 ± 0.01	7.97 ± 0.04	-1.52 ± 0.04
135036	45.43 ± 0.04	8.48 ± 0.21	-1.16 ± 0.17
44872	43.71 ± 0.01	7.97 ± 0.08	-2.36 ± 0.08
134539	–	–	–
133581	44.53 ± 0.01	7.81 ± 0.04	-1.38 ± 0.04
46186	44.90 ± 0.03	–	–
133141	44.82 ± 0.02	8.15 ± 0.05	-1.44 ± 0.05
132335	–	–	–
132310	45.73 ± 0.05	8.51 ± 0.04	-0.88 ± 0.06
132768	43.59 ± 0.01	–	–
133094	–	–	–
133299	46.28 ± 0.07	–	–
132336	44.02 ± 0.01	–	–
53113	–	–	–
132128	–	–	–
132658	–	–	–
132883	44.31 ± 0.01	–	–

<sup>a</sup> Representative  $L_{\text{bol}}$  and  $M_{\text{BH}}$  values (see Sections 4.1 and 4.2).

<sup>a</sup> The listed values do not include the intrinsic rms scatters of the  $L_{\text{bol}}$  and  $M_{\text{BH}}$  estimators, which are  $\sim 0.13$  dex and  $\sim 0.23$  dex, respectively.

NOTE—Column (1): *AKARI* ID. Column (2): Logarithmic bolometric luminosity in units of  $\text{erg s}^{-1}$ . Column (3): Logarithmic BH mass in units of  $M_{\odot}$ . Column (4): Logarithmic Eddington ratio. This table is fully available in a machine-readable format.

**Table 3.** Coefficients of  $L_{\text{MIR}}$ -based  $M_{\text{BH}}$  estimators

No.	$L_{\text{Cont}}$	$\text{FWHM}_{\text{Line}}$	$\alpha$
A	$L_{3.4}$	C IV	6.503±0.172
B	$L_{3.4}$	Mg II	6.939±0.116
C	$L_{3.4}$	H $\beta$	6.906±0.023
D	$L_{3.4}$	H $\alpha$	6.964±0.060
E	$L_{4.6}$	C IV	6.512±0.172
F	$L_{4.6}$	Mg II	6.948±0.116
G	$L_{4.6}$	H $\beta$	6.914±0.023
H	$L_{4.6}$	H $\alpha$	6.973±0.060

NOTE—For all lines,  $\beta$  is 0.478±0.016, while  $\gamma$  is 2 for H $\beta$  and 2.06±0.06 for the others.

the Mg II and/or C IV lines from Bisogni et al. (2017). Bisogni et al. (2017) obtained optical to NIR spectra simultaneously for six quasars at  $z\sim 2.2$  using the X-shooter spectrograph on the Very Large Telescope, and

derived the following relations:

$$\begin{aligned} & \log\left(\frac{\text{FWHM}_{\text{H}\alpha}}{1000 \text{ km s}^{-1}}\right) \\ &= \log\left(\frac{\text{FWHM}_{\text{Mg II}}}{1000 \text{ km s}^{-1}}\right) - (0.012 \pm 0.048) \end{aligned} \quad (5)$$

and

$$\begin{aligned} & \log\left(\frac{\text{FWHM}_{\text{H}\alpha}}{1000 \text{ km s}^{-1}}\right) \\ &= \log\left(\frac{\text{FWHM}_{\text{C IV}}}{1000 \text{ km s}^{-1}}\right) - (0.224 \pm 0.078). \end{aligned} \quad (6)$$

The obtained  $M_{\text{BH}}$  estimators based on the Mg II line are summarized as B and F in Table 3, while those based on the C IV line are listed as A and E.

Note that the H $\alpha$ -based  $M_{\text{BH}}$  estimator (Kim et al. 2023) has an rms scatter of 0.204 dex. Considering the  $\sim 0.11$  dex scatter in FWHM measurements between different emission lines as described in Section 3.2, the intrinsic scatters of the BH mass estimators in Table 3 become  $\sim 0.23$  dex.

Using these  $M_{\text{BH}}$  estimators, we derived BH masses for 212, 352, 64, and 37 objects using the C IV, Mg II, H $\beta$ , and H $\alpha$  lines, respectively. As with the representative  $L_{\text{bol}}$  values described in Section 4.1, we constructed representative  $M_{\text{BH}}$  values for each object by combining the available measurements. Since the  $L_{3.4}$  and  $L_{4.6}$  values were derived from a common SED fit, the resulting  $M_{\text{BH}}$  estimates are identical and were treated as a single measurement. Furthermore, when multiple line-based estimates are available, we prioritized those derived from the H $\beta$  line, followed by the Mg II, H $\alpha$ , and C IV lines. The representative BH masses, listed in Table 2, were obtained for 447 objects and span a wide range from  $10^{7.29}$  to  $10^{9.67} M_{\odot}$ . The mean and median  $M_{\text{BH}}$  values are  $10^{8.65}$  and  $10^{8.67} M_{\odot}$ , respectively, and the standard deviation is 0.42 dex. Note that the uncertainties in the  $M_{\text{BH}}$  values were estimated by taking into account the uncertainties of the  $L_{\text{MIR}}$  and FWHM measurements, together with those in the parameters of the  $M_{\text{BH}}$  estimators.

### 4.3. Eddington Ratio

In this subsection, we derived the Eddington ratios (hereafter,  $\lambda_{\text{Edd}}$ ) defined as  $\lambda_{\text{Edd}} \equiv L_{\text{bol}}/L_{\text{Edd}}$ , where  $L_{\text{Edd}}$  is the Eddington luminosity. We used the representative values of  $L_{\text{bol}}$  and  $M_{\text{BH}}$  to compute the  $\lambda_{\text{Edd}}$  values, resulting in measurements for 447 objects. The measured  $\lambda_{\text{Edd}}$  values are summarized in Table 2.

Figure 4 presents the distributions of  $L_{\text{bol}}$  and  $M_{\text{BH}}$ , with reference lines corresponding to  $\lambda_{\text{Edd}} = 1, 0.1, \text{ and } 0.01$ . All of the derived  $\lambda_{\text{Edd}}$  values are lower than 1,

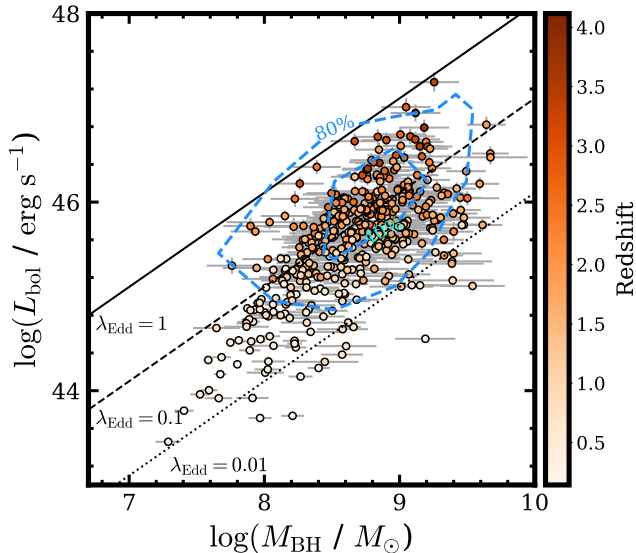


**Figure 4.** Distribution of BH masses and bolometric luminosities. Circles represent the representative BH masses and bolometric luminosities of Type-1 AGNs in the NEP-Wide field; their colors indicate redshift. Blue dashed contours indicate the distribution of SDSS DR14 quasars. The solid, dashed, and dotted lines correspond to  $\lambda_{\text{Edd}}$  values of 1.0, 0.1, and 0.01, respectively.

with  $\log(\lambda_{\text{Edd}})$  ranging from -2.74 to -0.08. The mean and median  $\log(\lambda_{\text{Edd}})$  values are -1.17 and -1.12, respectively, and the standard deviation is 0.43 dex. Moreover, the  $\lambda_{\text{Edd}}$  distributions of our sample is broadly consistent with that of the SDSS DR14 quasars, as shown in Figure 4.

## 5. DISCUSSION

### 5.1. Prevalence of Dust-obscured AGNs

The fraction of dust-obscured AGNs provides key insights into the cosmic evolution of both dust-obscured and unobscured AGN populations. Moreover, a substantial dust-obscured fraction (i) suggests the existence of a significant population of AGNs that have been missed in optical AGN surveys, and (ii) underscores the critical importance of correcting dust extinction when investigating the nature of AGNs (e.g., Kim et al. 2023; Kim & Im 2025). Additionally, the dust-obscured fraction may provide indirect evidence for a connection between galaxy mergers and galaxy evolution (e.g., Hopkins et al. 2006; Kocevski et al. 2015; Kim et al. 2020; La Marca et al. 2024). Some X-ray-based studies have found the dust-obscured fraction to be  $\geq 50\%$  (e.g., Martínez-Sansigre et al. 2005), though this fraction can vary depending on the redshift and AGN luminosity (e.g., Akylas et al. 2006; Polletta et al. 2008; Peca et al. 2023). In addition, even optical-based AGN surveys

also have non-negligible dust-obscured fractions. For instance, Kim et al. (2023) reported that a significant fraction ( $\sim 15\%$ ) of SDSS quasars are dust-obscured, and that their  $L_{\text{bol}}$  values derived from the optical continuum luminosities can be underestimated by  $\sim 50\%$ .

In this subsection, we investigated the dust-obscured AGN fraction for the Type-1 AGNs in the NEP-Wide field. For this analysis, we used a sample of 639 objects with the  $E(B-V)$  values obtained from the SED fitting, as described in Section 3.1. Based on these  $E(B-V)$  values, we classified objects with  $E(B-V) > 0.1$  as dust-obscured AGNs, and those with  $E(B-V) \leq 0.1$  as unobscured AGNs. Note that we tried to test our dust-obscured AGN classification using the Balmer decrement. However, only three dust-obscured AGNs have both  $H\beta$  and  $H\alpha$  flux measurements. Moreover, two of them have  $E(B-V) \lesssim 0.2$ ; given that the rms scatter between  $E(B-V)$  derived from the Balmer decrement and that from SED fitting is  $\sim 0.2$ , we could not robustly validate our SED-based classification due to the small sample size.

Figure 5 shows the distribution of the  $E(B-V)$  values. As a result, 220 and 419 objects were classified as dust-obscured and unobscured AGNs, respectively, and the redshifts of the dust-obscured AGNs span a wide range from 0.20 to 3.38, as shown in Figure 6. Note that this  $E(B-V)$  criterion has been widely adopted in previous studies (e.g., Glikman et al. 2007; Kim et al. 2015a, 2023, 2024b). However, due to the significant uncertainties in  $E(B-V)$  measurements, some studies (e.g., Kim et al. 2018) adopted higher thresholds to classify dust-obscured AGNs.

Using these dust-obscured and unobscured AGNs, we estimated the dust-obscured fraction, defined as the number of dust-obscured AGNs divided by the total number of both dust-obscured and unobscured AGNs, and found a dust-obscured fraction of 34%. However, the dust-obscured fraction can vary depending on how dust-obscured AGNs are defined. Kim et al. (2023) defined dust-obscured AGNs as those whose extinction-corrected  $L_{\text{bol}}$  is more than 1.5 times the  $L_{\text{bol}}$  derived from the uncorrected L5100. Using this definition, objects with  $E(B-V) \gtrsim 0.13$  are classified as dust-obscured AGNs, and the corresponding dust-obscured fraction decreases to  $\sim 28\%$ . This fraction is still higher than that of the SDSS quasars (Kim et al. 2023), which is 16%. While this discrepancy can result from various factors such as photometric depth and the definition of the dust-obscured fraction, (i) the optical-to-IR color-based sample selection adopted in the DESI and (ii) the tendency of *AKARI*-detected AGNs to favor a more obscured population are suspected to be the primary fac-

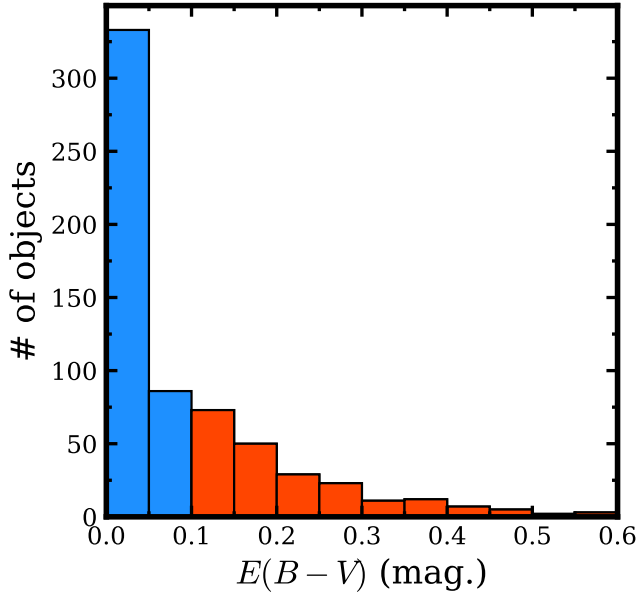


**Figure 5.** Distribution of  $E(B - V)$  values derived from SED fitting. The blue and red histograms represent unobscured [ $E(B - V) \leq 0.1$ ] and dust-obscured [ $E(B - V) > 0.1$ ] AGNs, respectively.

tors. Furthermore, Kim et al. (2018) reported that the typical rms scatter in the  $E(B - V)$  measurements is  $\sim 0.2$ , which could have introduced a minor bias into the derived dust-obscured fraction.

Although the significant dust-obscured fraction was found among the Type-1 AGNs detected in the optical and MIR surveys, this estimate may still suffer from various selection biases, particularly as heavily obscured AGNs tend to be missed. To mitigate such biases, we further estimated the dust-obscured fraction using a subsample of X-ray detected objects from our sample. The NEP-Deep field, located within the NEP-Wide field, was observed by a 300 ks *Chandra* survey (Krumpe et al. 2015). This survey detected 457 X-ray sources, of which 33 were matched to our sample with available  $E(B - V)$  measurements. Based on the X-ray detected AGNs, we derived a dust-obscured fraction of 27%. Furthermore, considering the AGNs detected in the hard X-ray (2–7 keV) band, we obtained a comparable fraction of 30%. These estimates are broadly consistent with the dust-obscured fraction obtained from the optical-MIR detected AGNs.

To further examine the dust-obscured fraction as a function of redshift, we selected AGNs with bolometric luminosities in the range  $10^{44.5} - 10^{46.5} \text{ erg s}^{-1}$ , yielding a sample of 569 objects (206 dust-obscured and 363 unobscured AGNs), which is sufficiently large to provide statistically robust results. To alleviate luminosity-dependent biases, we further divided

this sample into four  $L_{\text{bol}}$  bins:  $10^{44.5} - 10^{45.0} \text{ erg s}^{-1}$ ,  $10^{45.0} - 10^{45.5} \text{ erg s}^{-1}$ ,  $10^{45.5} - 10^{46.0} \text{ erg s}^{-1}$ , and  $10^{46.0} - 10^{46.5} \text{ erg s}^{-1}$ . Within these  $L_{\text{bol}}$  bins, 14, 67, 98, and 27 dust-obscured AGNs were selected, while 60, 112, 123, and 68 unobscured AGNs were chosen, respectively.

For these subsamples, the derived dust-obscured fractions are comparable, as shown in Figure 7. Since there are only a few AGNs in some redshift bins, bins fewer than 10 objects are not presented in Figure 7. The dust-obscured fraction is typically  $\sim 40\%$  (ranging from  $\sim 10\%$  to  $\sim 65\%$ ) in the redshift range  $0.5 < z < 2.0$ , which is consistent with several previous studies (e.g., Akylas et al. 2006). The subsamples with  $L_{\text{bol}}$  between  $10^{45.0} - 10^{45.5} \text{ erg s}^{-1}$  and  $10^{45.5} - 10^{46.0} \text{ erg s}^{-1}$  exhibit no clear redshift-dependent trend in the dust-obscured fraction. In contrast, the subsamples with  $L_{\text{bol}}$  in the ranges  $10^{44.5} - 10^{45.0} \text{ erg s}^{-1}$  and  $10^{46.0} - 10^{46.5} \text{ erg s}^{-1}$  show a declining trend beyond  $z \gtrsim 0.5$  and  $z \gtrsim 1.5$ , respectively. Such a trend needs to be verified with a larger sample, given the limited number of dust-obscured AGNs in these bins ( $< 10$  objects in each bin) and the potential effects of selection biases. Note that even when using subsamples with narrower  $L_{\text{bol}}$  or redshift bins, no significant new trends were revealed.

Note that, since the DESI quasars were selected based on the optical-to-IR colors, the sample cannot be considered complete for dust-obscured objects. Consequently, the redshift trends could be biased. As spectroscopic surveys of the NEP-Wide field become more complete through SPHEREx and other upcoming missions, both the number and completeness of identified dust-obscured AGNs will increase, leading to more statistically robust and comprehensive results for the dust-obscured fraction and its redshift dependence.

## 5.2. Spectral Energy Distribution of Dust-obscured AGNs

We compared the SED shapes of the dust-obscured and unobscured AGNs. The SEDs for all AGNs were constructed from the multi-band photometry used in Section 3.1. Owing to the closely spaced wavelengths of the *AKARI*, *WISE*, and *Spitzer* IR photometric data points, such photometry provides an ideal data set for SED shape analysis in the IR region. Using the *K*-band wavelength, where the effect of dust extinction is expected to be minimal, as the reference point, we normalized the SEDs and then median-combined them within each type for comparison. The 16th and 84th percentiles of the combined SEDs were used as the  $1\sigma$  confidence level.

The comparison of the SED shapes for the dust-obscured and unobscured AGNs is presented in Figure

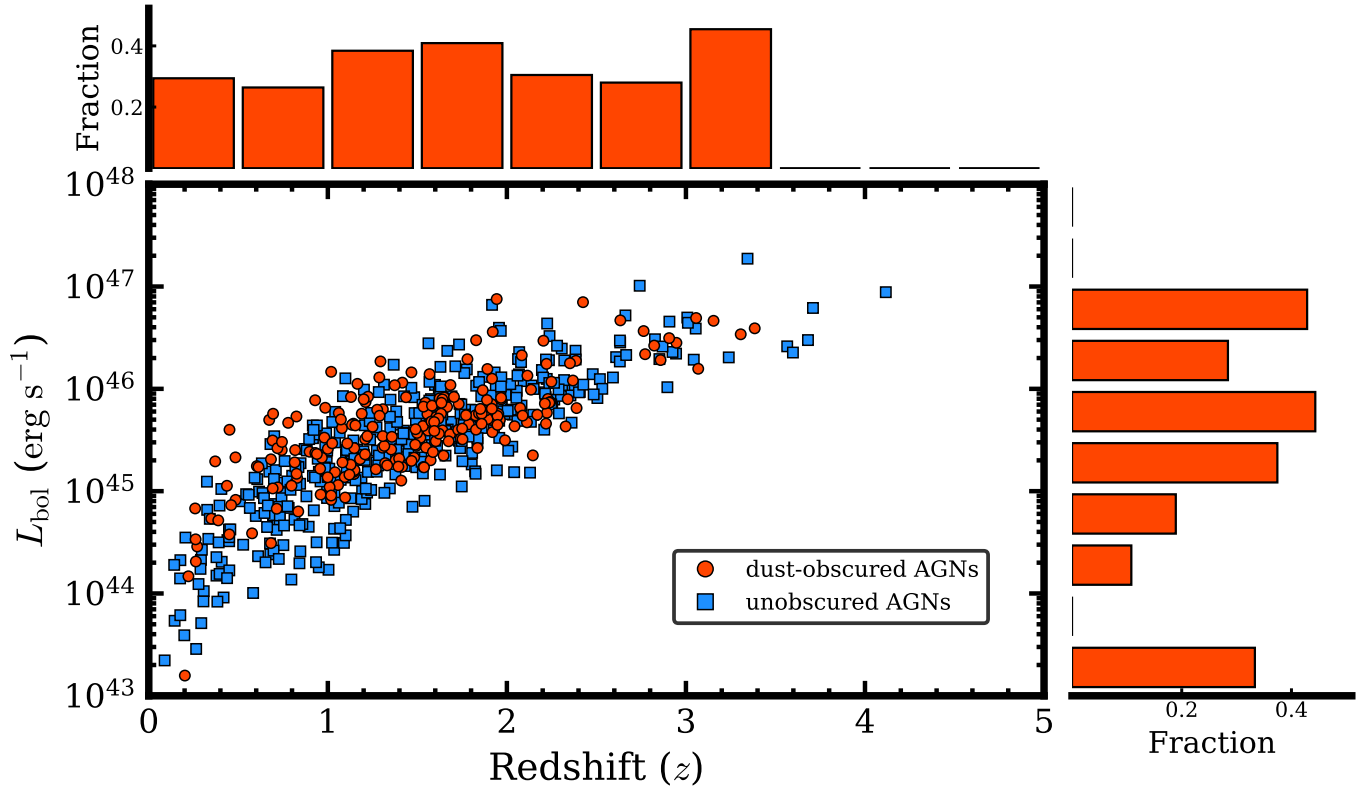


**Figure 6.** Distributions of bolometric luminosity versus redshift for dust-obscured and unobscured AGNs. Red circles and blue squares represent dust-obscured and unobscured AGNs, respectively. The top and right panels show the redshift and bolometric luminosity distributions of the dust-obscured fraction, respectively.

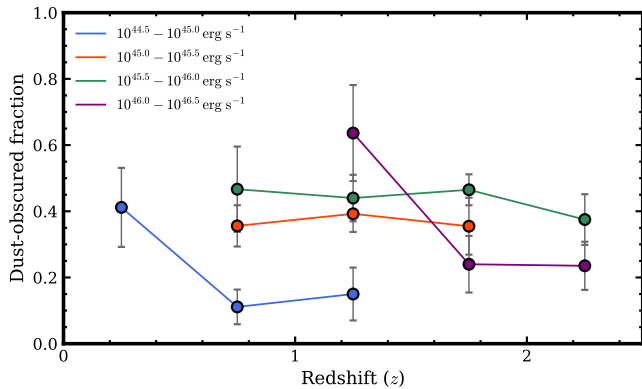


**Figure 7.** Dust-obscured AGN fraction as a function of redshift in four bolometric luminosity subsamples. The blue, red, green, and purple circles and lines denote the fractions for  $L_{\text{bol}}$  ranges of  $10^{44.5}-10^{45.0}$ ,  $10^{45.0}-10^{45.5}$ ,  $10^{45.5}-10^{46.0}$ , and  $10^{46.0}-10^{46.5}$ , respectively. Only cases where the number of AGNs is at least ten are shown to avoid the effects of small number statistics.

8. In the optical region, they differ significantly: at  $5100 \text{ \AA}$ , the combined SED of the unobscured AGNs is 57% higher than that of the dust-obscured AGNs. Considering the  $1\sigma$  confidence level for the combined SED of the dust-obscured AGNs (37%), this difference between

the two types is statistically significant. Furthermore, by dividing the dust-obscured AGNs into moderately obscured ( $0.1 < E(B - V) \leq 0.2$ ) and heavily obscured ( $E(B - V) > 0.2$ ) AGNs, we find that the SED differences relative to the unobscured AGNs become more pronounced as  $E(B - V)$  increases. In contrast, in the IR region at wavelengths of  $3.4 \mu\text{m}$  and  $4.6 \mu\text{m}$ , the combined SED of the unobscured AGNs is 91% and 92% of that of the dust-obscured AGNs, differences that are not statistically significant given the corresponding  $1\sigma$  uncertainties of 18% and 25%, respectively. Moreover, the overall IR SED shapes of the two AGN populations show no substantial differences, nor do they exhibit any noticeable change with increasing  $E(B - V)$ .

Since (i) the IR SED shapes can be affected by dust torus properties (e.g., Kim et al. 2015b; Son et al. 2023) and (ii) the geometry of the dust torus is known to be related to luminosity (e.g., Toba et al. 2013; Kim et al. 2024c), we restricted our sample to AGNs with  $L_{\text{bol}}$  in the range of  $10^{45}-10^{46} \text{ erg s}^{-1}$  and compared their SED shapes. Figure 8 presents the SED shapes for the  $L_{\text{bol}}$ -limited dust-obscured and unobscured AGNs, and the overall trends are broadly consistent with those obtained from the entire sample. In addition, a similar analy-

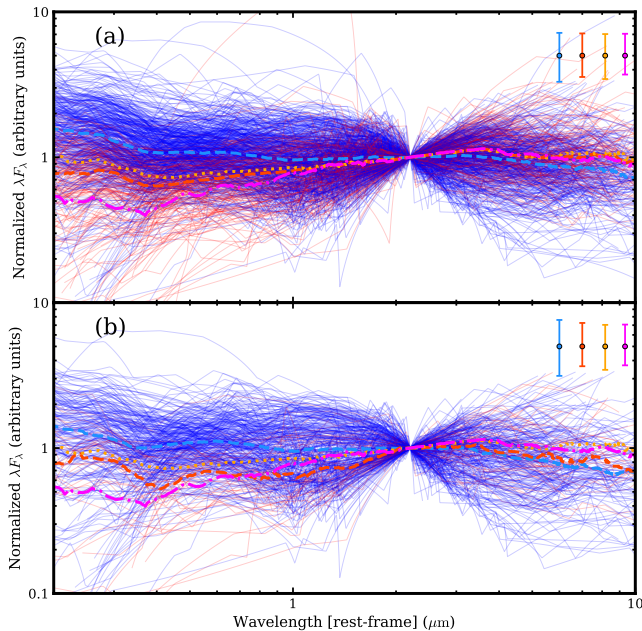


**Figure 8.** Normalized SED shapes of dust-obscured and unobscured AGNs. Panels (a) and (b) show the entire AGN sample and those of AGNs with  $L_{\text{bol}}$  in the range of  $10^{45}$ – $10^{46}$   $\text{erg s}^{-1}$ , respectively. Red and blue solid lines represent individual dust-obscured and unobscured AGN SEDs, respectively, normalized at the  $K$ -band wavelength. The red and blue dashed lines indicate the median-combined SEDs for the two populations. The orange dotted and magenta dot-dashed lines represent the median-combined SEDs of moderately obscured ( $0.1 < E(B - V) < 0.2$ ) and heavily obscured ( $E(B - V) > 0.2$ ) AGNs, respectively. The red and blue error bars in the top-right corner show the representative  $1\sigma$  confidence levels of the combined SED shapes for dust-obscured and unobscured AGNs, respectively. The orange and magenta error bars correspond to the same confidence levels for the moderately and heavily obscured AGN subsamples, respectively.

sis performed for the moderately obscured and heavily obscured AGN subsamples yielded results in agreement with the same trend.

The optical SED shapes of the dust-obscured AGNs are thought to be affected by dust extinction, whereas the similarity of their IR SED shapes to those of the unobscured AGNs suggests that dust torus properties such as the covering factor and the inclination angle are not significantly different between the two AGN populations. This similarity further provides strong support for the applicability of the  $L_{\text{MIR}}$ -based  $L_{\text{bol}}$  and  $M_{\text{BH}}$  estimators (Kim et al. 2023), established with unobscured AGNs, to dust-obscured AGNs.

### 5.3. Dust Extinction Correction: A Key Element in AGN Studies

Consistent with previous X-ray-based studies (e.g., Martínez-Sansigre et al. 2005), we found that the Type-1 AGNs in the NEP-Wide field exhibit a substantial ( $\sim 35\%$ ) dust-obscured fraction. Moreover, even SDSS quasars, which are typically regarded as relatively unaffected by dust extinction, show a non-negligible dust-obscured fraction of  $\sim 15\%$  (Kim et al. 2023). These results suggest that dust extinction can significantly affect a substantial fraction of AGNs, including those selected from optical AGN surveys that are generally considered unobscured. Therefore, as emphasized by Kim & Im (2025), correcting for dust extinction should be considered as a fundamental step in AGN studies, even for optically selected sources.

In this subsection, we investigated how the use of UV or optical continuum luminosities without extinction correction can lead to an underestimation of bolometric luminosities. For this purpose, we derived  $L_{\text{bol}}$  values using UV/optical continuum luminosity-based estimators without applying dust extinction correction, and compared them with our  $L_{\text{MIR}}$ -based  $L_{\text{bol}}$  values. To derive the  $L_{\text{bol}}$  values from UV/optical continuum luminosities, we measured the monochromatic continuum luminosities at 1450 Å, 3000 Å, and 5100 Å (hereafter, L1450, L3000, and L5100, respectively), which have been widely used as proxies for  $L_{\text{bol}}$  (e.g., Runnoe et al. 2012; Chen et al. 2025). These UV/optical luminosities were measured using the PyQSOFit code applied to the DESI DR1 and Shim et al. (2013) spectra, after correcting for Galactic dust extinction.

Using these UV/optical continuum luminosities, we derived  $L_{\text{bol}}$  values based on the empirical linear relations from Chen et al. (2025). For a direct comparison with the  $L_{\text{bol}}$  values obtained using the  $L_{\text{MIR}}$ -based estimators from Kim et al. (2023), who defined  $L_{\text{bol}}$  as the integrated luminosity from 10 KeV to  $1 \mu\text{m}$ , we adopted the linear relations derived for  $L_{\text{bol}}$  over the same wavelength range.

Note that L1450– $L_{\text{bol}}$  relation is sensitive to variations in SED shapes; consequently, various L1450-based  $L_{\text{bol}}$  estimators (e.g., Shen et al. 2011; Runnoe et al. 2012; Chen et al. 2025) can yield noticeably different values. This sensitivity to SED shapes may arise from object-to-object differences in the UV bump, whose peak position can vary significantly among AGNs depending on the accretion disk temperature, inclination, and BH mass (e.g., Malkan 1983; Czerny & Elvis 1987; Scott et al. 2004). Hence, for SDSS quasars, the fractional residual, defined as  $\left| \frac{L_{\text{bol}(\text{model})} - L_{\text{bol}(\text{true})}}{L_{\text{bol}(\text{true})}} \right|$ , has been found to be 34 times larger for L1450 than for L3000, and 2.4 times larger than for L5100 (Chen et al. 2025). Therefore, L1450-based  $L_{\text{bol}}$  estimators yield different results; for

instance, if we adopted the L1450-based estimator from [Runnoe et al. \(2012\)](#), the derived  $L_{\text{bol}}$  values would increase by a factor of  $\sim 1.71$ .

Moreover, to clearly examine the role of dust extinction correction in the comparison, we restricted the effects from host galaxy contamination. Previous studies (e.g., [Shen et al. 2011](#); [Kim et al. 2023](#)) showed that host galaxy contributions are relatively minor (e.g.,  $\lesssim 20\%$ ) in the UV and MIR, compared to the optical and NIR. However, the L5100, as an optical continuum luminosity, can be significantly affected by host galaxy contamination, particularly in low-luminosity AGNs ([Shen et al. 2011](#); [Jalan et al. 2023](#)). Therefore, in our L5100-based analysis, we included only objects with  $L_{5100} > 10^{44.5} \text{ erg s}^{-1}$ , since the host galaxy contributions at this luminosity are expected to be limited ( $\lesssim 25\%$ ; [Shen et al. 2011](#); [Jalan et al. 2023](#); [Ren et al. 2024](#)). Note that, under such conditions, only 20 objects remain (6 dust-obscured and 14 unobscured AGNs), which is insufficient to obtain statistically robust results.

We compared the  $L_{\text{bol}}$  values derived from the  $L_{\text{MIR}}$  and the UV/optical continuum luminosities after dividing the sample into dust-obscured and unobscured AGNs, as shown in [Figure 9](#). However, note that the comparison with the L5100-based  $L_{\text{bol}}$  was omitted from [Figure 9](#) due to the limited number of objects. For the unobscured AGNs, the  $L_{\text{bol}}$  values estimated from UV/optical luminosities are broadly consistent with those derived from  $L_{\text{MIR}}$ , with  $\log[L_{\text{bol}}(\text{UV, opt})/L_{\text{bol}}(\text{MIR})] = -0.04 \pm 0.02$ ,  $-0.10 \pm 0.01$ , and  $0.09 \pm 0.06$ , for L1450, L3000, and L5100, respectively. In contrast, for the dust-obscured AGNs, the  $L_{\text{bol}}$  values based on L1450, L3000, and L5100 tend to be lower than those from  $L_{\text{MIR}}$ , with  $\log[L_{\text{bol}}(\text{UV, opt})/L_{\text{bol}}(\text{MIR})] = -0.46 \pm 0.06$ ,  $-0.46 \pm 0.02$ , and  $-0.12 \pm 0.09$ , respectively.

For dust-obscured AGNs, we applied extinction correction to the L3000 values, which is insensitive to SED shapes and not limited by small number statistics. By deriving  $L_{\text{bol}}$  values from the extinction-corrected L3000 values using the  $E(B - V)$  measurements, we found that the resulting  $L_{\text{bol}}$  values are consistent with the  $L_{\text{MIR}}$ -based  $L_{\text{bol}}$  values, yielding  $\log[L_{\text{bol}}(3000 \text{ \AA})/L_{\text{bol}}(\text{MIR})] = 0.03 \pm 0.02$ . These findings suggest that the underestimation of the L3000-based  $L_{\text{bol}}$  for dust-obscured AGNs arises from dust extinction. A more conclusive verification of this result would require accurate  $E(B - V)$  measurements, achievable through complementary analyses such as line ratio, X-ray hardness, and other diagnostics (e.g., [Kim & Im 2018](#)). However, such analyses are beyond the scope of this study.

Therefore, we concluded that the substantial fraction (34%) of dust-obscured AGNs among the Type-1 AGNs in the NEP-Wide field raises concerns that  $L_{\text{bol}}$  estimates may be significantly underestimated if UV continuum luminosities are used as  $L_{\text{bol}}$  estimators without dust extinction correction. Given the prevalence of dust-obscured AGNs across the entire AGN population, not just within the NEP-Wide field, our findings underscore that correcting for dust extinction is a crucial step in AGN studies.

#### 5.4. Eddington Ratios of Dust-obscured AGNs

In this subsection, we investigated whether dust-obscured AGNs exhibit higher  $\lambda_{\text{Edd}}$  values than unobscured AGNs. In the merger-driven galaxy evolution scenario ([Hopkins et al. 2008](#)), dust-obscured AGNs are expected to have higher  $\lambda_{\text{Edd}}$  values than unobscured AGNs ([Urrutia et al. 2012](#); [Kim et al. 2015a, 2024a,b](#)), and the extinction of dust-obscured AGNs arises from dust in their host galaxies. Alternatively, if the extinction of dust-obscured AGNs originates from the dust torus viewed at moderate inclinations ([Wilkes et al. 2002](#); [Rose et al. 2013](#)) in the orientation-based unification model, dust-obscured AGNs are expected to have similar  $\lambda_{\text{Edd}}$  values to unobscured AGNs.

Moreover, to examine the dependence of  $\lambda_{\text{Edd}}$  on  $E(B - V)$ , we divided the dust-obscured AGNs into two subsamples: moderately obscured ( $0.1 < E(B - V) \leq 0.2$ ) and heavily obscured ( $E(B - V) > 0.2$ ), following the classification in [Section 5.2](#), and compared their  $\lambda_{\text{Edd}}$  values with those of unobscured AGNs. Note that in this comparison, only the AGNs at  $z < 2.5$  were considered, where the number of dust-obscured AGNs is sufficient to yield statistically robust results.

For this comparison, we used 296 unobscured AGNs and 125 dust-obscured AGNs. Among the dust-obscured AGNs, 77 objects are the moderately obscured AGNs, and the remaining 48 objects are the heavily obscured AGNs.

The median  $\log(\lambda_{\text{Edd}})$  values of the unobscured and dust-obscured AGNs are  $-1.23 \pm 0.02$  and  $-1.16 \pm 0.04$ , respectively, over the entire redshift range. This result shows that the dust-obscured AGNs have slightly higher  $\lambda_{\text{Edd}}$  values than the unobscured AGNs. To quantify the significance of this difference, we performed a Kolmogorov-Smirnov (K-S) test using the SciPy ([Virtanen et al. 2020](#)) Python package. The maximum deviation between the cumulative distributions,  $D$ , is 0.13, and the corresponding  $p$ -value is 0.08, which suggests that the two distributions differ at a marginally significant level.

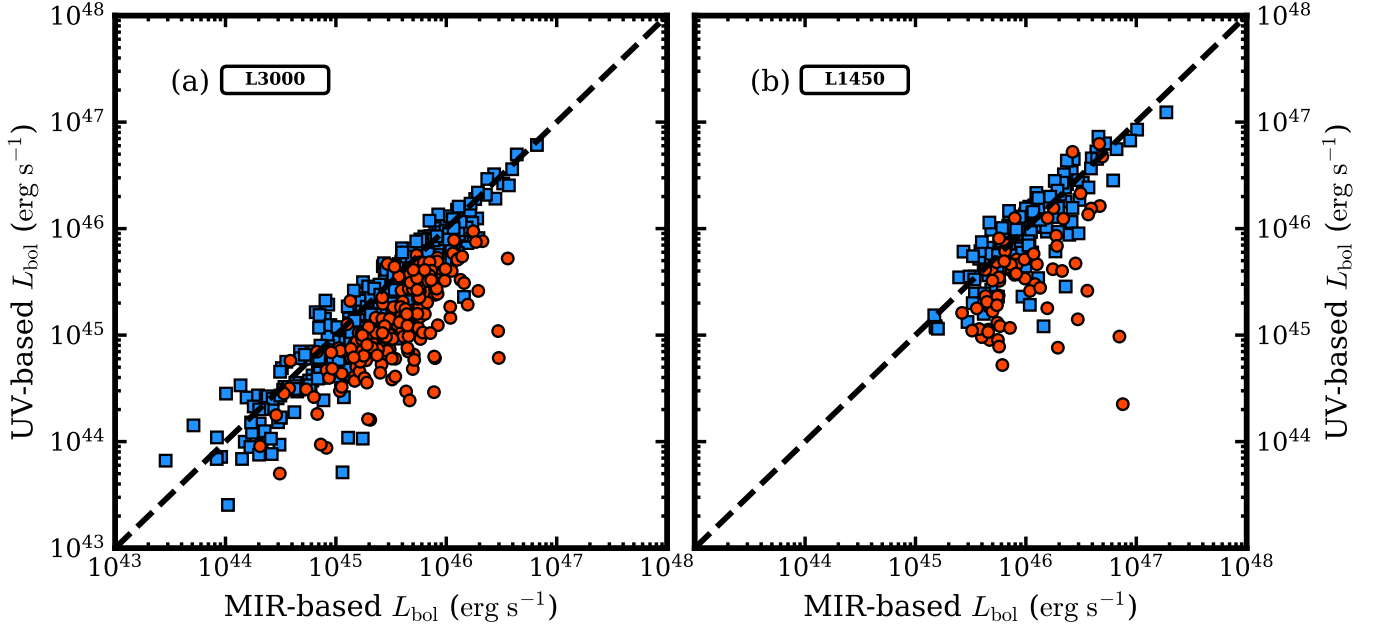


**Figure 9.** Comparison of bolometric luminosities from UV continuum luminosities and those from  $L_{\text{MIR}}$  values. Panels (a) and (b) compare the  $L_{\text{MIR}}$ -based  $L_{\text{bol}}$  values to those from L3000 and L1450, respectively. Red circles and blue squares represent dust-obscured and unobscured AGNs, respectively, and the one-to-one relations are shown as the dashed black lines.

Note that the median  $\log(\lambda_{\text{Edd}})$  values of the moderately obscured and heavily obscured AGNs are  $-1.18 \pm 0.04$  and  $-1.13 \pm 0.06$ , respectively. Moreover, we performed additional K-S tests comparing the two dust-obscured AGN subsamples with the unobscured AGNs. The resulting  $D$  values are 0.11 and 0.20, and the corresponding  $p$ -values are 0.43 and 0.05, respectively. These results suggest that (i) the  $\lambda_{\text{Edd}}$  values of dust-obscured AGNs are higher than those of the unobscured AGNs, and (ii) the difference increases with  $E(B-V)$ , although this trend is not statistically robust.

However, these  $\lambda_{\text{Edd}}$  comparisons can be affected by (i) sample bias or (ii) cosmological evolution. Therefore, we compared the  $\lambda_{\text{Edd}}$  values of the unobscured and dust-obscured AGNs as a function of redshifts. For this purpose, we divided the two AGN populations into eight redshift bins: 0.1–0.4, 0.4–0.7, 0.7–1.0, 1.0–1.3, 1.3–1.6, 1.6–1.9, 1.9–2.2, and 2.2–2.5. The median  $\log(\lambda_{\text{Edd}})$  values of the unobscured AGNs in these redshift bins are  $-1.61 \pm 0.41$ ,  $-1.62 \pm 0.44$ ,  $-1.29 \pm 0.35$ ,  $-1.33 \pm 0.37$ ,  $-1.09 \pm 0.31$ ,  $-1.06 \pm 0.33$ ,  $-0.94 \pm 0.33$ , and  $-1.03 \pm 0.35$ , whereas those of the dust-obscured AGNs are  $-1.43 \pm 0.35$ ,  $-1.23 \pm 0.31$ ,  $-1.31 \pm 0.42$ ,  $-1.09 \pm 0.35$ ,  $-1.21 \pm 0.33$ ,  $-1.21 \pm 0.40$ ,  $-0.92 \pm 0.32$ , and  $-0.94 \pm 0.32$ . These results suggest that although both the unobscured and the dust-obscured AGNs exhibit an increasing trend in  $\lambda_{\text{Edd}}$  with redshift, the difference in  $\lambda_{\text{Edd}}$  between the two populations is not statistically strong.

Furthermore, the redshift dependence of  $\lambda_{\text{Edd}}$  was investigated for the two dust-obscured AGN subsamples. The median  $\log(\lambda_{\text{Edd}})$  values of the moderately obscured AGNs in the redshift bins are  $-1.79 \pm 0.00$ ,  $-1.50 \pm 0.28$ ,  $-1.31 \pm 0.31$ ,  $-1.07 \pm 0.32$ ,  $-1.32 \pm 0.23$ ,  $-1.34 \pm 0.38$ ,  $-0.92 \pm 0.25$ , and  $-0.94 \pm 0.35$ , while those of the heavily obscured AGNs are  $-1.29 \pm 0.35$ ,  $-1.20 \pm 0.26$ ,  $-1.39 \pm 0.54$ ,  $-1.35 \pm 0.41$ ,  $-0.96 \pm 0.49$ ,  $-1.06 \pm 0.40$ ,  $-0.64 \pm 0.39$ , and  $-0.81 \pm 0.23$ . These results show that the  $\lambda_{\text{Edd}}$  values of the moderately obscured AGNs are comparable to those of the unobscured AGNs. In contrast, the heavily obscured AGNs exhibit somewhat higher  $\lambda_{\text{Edd}}$  values, although the difference is not statistically robust.

These comparisons are presented in Figure 10. We do not find statistically robust evidence for an increase in  $\lambda_{\text{Edd}}$  with  $E(B-V)$ , consistent with an orientation-based interpretation in which moderate obscuration arises from a dust torus viewed at intermediate inclination (e.g., Wilkes et al. 2002; Rose et al. 2013). In contrast, the heavily obscured AGNs may exhibit higher  $\lambda_{\text{Edd}}$  values than the other populations, consistent with previous studies (e.g., Urrutia et al. 2012; Kim et al. 2015a, 2024a,b). This suggests that their dust extinction may arise from dust in the host galaxies.

## 6. SUMMARY

We derived the BH properties of 861 Type-1 AGNs in the NEP-Wide field using the  $L_{\text{MIR}}$  values at  $3.4 \mu\text{m}$  and  $4.6 \mu\text{m}$ , combined with the FWHM values of the

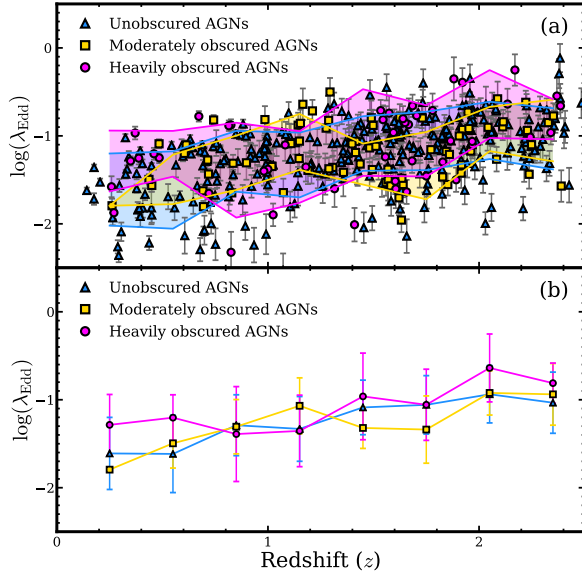


**Figure 10.**  $\log(\lambda_{\text{Edd}})$  values versus redshifts. Blue triangles, yellow squares, and magenta circles correspond to unobscured ( $E(B - V) \leq 0.1$ ), moderately obscured ( $0.1 < E(B - V) \leq 0.2$ ), and heavily obscured ( $E(B - V) > 0.2$ ) AGNs, respectively. (a) Colored polygons indicate the median  $\log(\lambda_{\text{Edd}})$  and  $1\sigma$  dispersions in eight redshift bins. (b) Median  $\log(\lambda_{\text{Edd}})$  values in the same eight redshift bins are shown with  $1\sigma$  dispersions.

C IV, Mg II,  $H\beta$ , and  $H\alpha$  lines. By performing SED and line fitting, we obtained the  $L_{\text{MIR}}$  and FWHM values. From these measurements, we derived the  $L_{\text{bol}}$ ,  $M_{\text{BH}}$ , and  $\lambda_{\text{Edd}}$  values, which are less affected by dust extinction due to the use of the extinction-corrected  $L_{\text{MIR}}$  values. We found that 34% of the Type-1 AGNs in the NEP-Wide field are dust obscured, which can lead to significant underestimation of their  $L_{\text{bol}}$  values if UV luminosities are used as proxies for  $L_{\text{bol}}$  without applying proper extinction correction. These findings underscore the importance of correcting for dust extinction in AGN studies. As ongoing and upcoming IR spectroscopic missions, such as SPHEREx and *Euclid*, begin to cover the NEP-Wide field, our measurements will serve as fiducial BH properties for future AGN studies. This paper represents the first step of our project, focusing on AGNs detected in both optical and MIR surveys. In forthcoming studies (Papers II and III), we will extend our analysis to AGNs detected only in the optical survey and only in the MIR survey, respectively.

1 We thank the anonymous referee for the useful com-  
 2 ments. D.K. acknowledges the support by the Na-  
 3 tional Research Foundation of Korea (NRF) grant (No.  
 4 2021R1C1C1013580 and 2022R1A4A3031306) funded  
 5 by the Korean government (MSIT). M.I. acknowledges  
 6 the support from the National Research Foundation of  
 7 Korea (NRF) grant, No. 2021M3F7A1084525, funded  
 8 by the Korea government (MSIT). H.S. acknowledges  
 9 the support from the National Research Foundation of  
 10 Korea (NRF) grant funded by the Korea government  
 11 (MSIT) (No. RS-2024-00349364). Y.K. was supported  
 12 by the National Research Foundation of Korea (NRF)  
 13 grant funded by the Korean government (MSIT) (No.  
 14 2021R1C1C2091550).

15 We are grateful to Jie Chen for providing the linear  
 16 relations between  $L_{\text{bol}}$  values and the UV/optical con-  
 17 tinuum luminosities, which greatly contributed to this  
 18 study.

## REFERENCES

- Akylas, A., Georgantopoulos, I., Georgakakis, A., et al. 2006, *A&A*, 459, 3, 693. doi:10.1051/0004-6361:20054632
- Alexander, D. M., Davis, T. M., Chaussidon, E., et al. 2023, *AJ*, 165, 3, 124. doi:10.3847/1538-3881/acacfc
- Assef, R. J., Kochanek, C. S., Brodwin, M., et al. 2010, *ApJ*, 713, 2, 970. doi:10.1088/0004-637X/713/2/970
- Barden, S. C., Armandroff, T., Muller, G., et al. 1994, *Proc. SPIE*, Modifying Hydra for the WIYN telescope: an optimum telescope, fiber MOS combination, 2198, 87. doi:10.1117/12.176816
- Bisogni, S., di Serego Alighieri, S., Goldoni, P., et al. 2017, *A&A*, 603, A1. doi:10.1051/0004-6361/201630143
- Brown, M. J. I., Jarrett, T. H., & Cluver, M. E. 2014, *PASA*, 31, e049. doi:10.1017/pasa.2014.44
- Burgarella, D., Mazyed, F., Oi, N., et al. 2019, *PASJ*, AKARI NEP field: Point source catalogs from GALEX and Herschel observations and selection of candidate lensed sub-millimeter galaxies, 71, 1, 12. doi:10.1093/pasj/psy134
- Busca, N. & Balland, C. 2018, , arXiv:1808.09955. doi:10.48550/arXiv.1808.09955
- Calzetti, D., Armus, L., Bohlin, R. C., et al. 2000, *ApJ*, 533, 2, 682. doi:10.1086/308692
- Cardelli, J. A., Clayton, G. C., & Mathis, J. S. 1989, *ApJ*, 345, 245. doi:10.1086/167900
- Chaussidon, E., Yèche, C., Palanque-Delabrouille, N., et al. 2023, *ApJ*, 944, 1, 107. doi:10.3847/1538-4357/acb3c2
- Chen, J., Jiang, L., Sun, S., et al. 2025, *ApJ*, 988, 2, 204. doi:10.3847/1538-4357/ade307
- Czerny, B. & Elvis, M. 1987, *ApJ*, 321, 305. doi:10.1086/165630
- DESI Collaboration, Aghamousa, A., Aguilar, J., et al. 2016, , The DESI Experiment Part I: Science, Targeting, and Survey Design, arXiv:1611.00036. doi:10.48550/arXiv.1611.00036
- DESI Collaboration, Aghamousa, A., Aguilar, J., et al. 2016, , The DESI Experiment Part II: Instrument Design, arXiv:1611.00037. doi:10.48550/arXiv.1611.00037
- DESI Collaboration, Abdul-Karim, M., Adame, A. G., et al. 2025, , Data Release 1 of the Dark Energy Spectroscopic Instrument, arXiv:2503.14745. doi:10.48550/arXiv.2503.14745
- Dey, A., Schlegel, D. J., Lang, D., et al. 2019, *AJ*, 157, 5, 168. doi:10.3847/1538-3881/ab089d
- Doré, O., Werner, M. W., Ashby, M., et al. 2016, , Science Impacts of the SPHEREx All-Sky Optical to Near-Infrared Spectral Survey: Report of a Community Workshop Examining Extragalactic, Galactic, Stellar and Planetary Science, arXiv:1606.07039. doi:10.48550/arXiv.1606.07039
- Doré, O., Werner, M. W., Ashby, M. L. N., et al. 2018, , Science Impacts of the SPHEREx All-Sky Optical to Near-Infrared Spectral Survey II: Report of a Community Workshop on the Scientific Synergies Between the SPHEREx Survey and Other Astronomy Observatories, arXiv:1805.05489. doi:10.48550/arXiv.1805.05489
- Euclid Collaboration, Scaramella, R., Amiaux, J., et al. 2022, *A&A*, Euclid preparation. I. The Euclid Wide Survey, 662, A112. doi:10.1051/0004-6361/202141938
- Euclid Collaboration, Mellier, Y., Abdurro'uf, et al. 2025, *A&A*, Euclid: I. Overview of the Euclid mission, 697, A1. doi:10.1051/0004-6361/202450810
- Fabricant, D. G., Kurtz, M. J., Geller, M. J., et al. 2008, *PASP*, Spectrophotometry with Hectospec, the MMT's Fiber-Fed Spectrograph, 120, 873, 1222. doi:10.1086/593023
- Galametz, A., Saglia, R., Paltani, S., et al. 2017, *A&A*, 598, A20. doi:10.1051/0004-6361/201629333
- Glikman, E., Helfand, D. J., White, R. L., et al. 2007, *ApJ*, 667, 2, 673. doi:10.1086/521073
- Greene, J. E. & Ho, L. C. 2005, *ApJ*, 630, 1, 122. doi:10.1086/431897
- Guo, H., Shen, Y., & Wang, S. 2018, *Astrophysics Source Code Library*. ascl:1809.008
- Henry, J. P., Mullis, C. R., Voges, W., et al. 2006, *ApJS*, The ROSAT North Ecliptic Pole Survey: The X-Ray Catalog, 162, 2, 304. doi:10.1086/498749
- Hopkins, P. F., Hernquist, L., Cox, T. J., et al. 2006, *ApJS*, 163, 1, 1. doi:10.1086/499298
- Hopkins, P. F., Hernquist, L., Cox, T. J., et al. 2008, *ApJS*, 175, 2, 356. doi:10.1086/524362
- Huang, T.-C., Matsuhara, H., Goto, T., et al. 2020, *MNRAS*, 498, 1, 609. doi:10.1093/mnras/staa2459
- Hwang, N., Lee, M. G., Lee, H. M., et al. 2007, *ApJS*, An Optical Source Catalog of the North Ecliptic Pole Region, 172, 2, 583. doi:10.1086/519216
- Im, M., Griffiths, R. E., & Ratnatunga, K. U. 1997, *ApJ*, A Measurement of the Cosmological Constant Using Elliptical Galaxies as Strong Gravitational Lenses, 475, 2, 457. doi:10.1086/303583

- Im, M.-S., Ko, J.-W., Cho, Y.-S., et al. 2010, *Journal of Korean Astronomical Society*, Seoul National University 4K×4K Camera (snucam) for Maidanak Observatory, 43, 3, 75. doi:10.5303/JKAS.2010.43.3.075
- Jalan, P., Rakshit, S., Woo, J.-J., et al. 2023, *MNRAS*, 521, 1, L11. doi:10.1093/mnras/slad014
- Jarrett, T. H., Cohen, M., Masci, F., et al. 2011, *ApJ*, The Spitzer-WISE Survey of the Ecliptic Poles, 735, 2, 112. doi:10.1088/0004-637X/735/2/112
- Jeon, Y., Im, M., Ibrahimov, M., et al. 2010, *ApJS*, Optical Images and Source Catalog of AKARI North Ecliptic Pole Wide Survey Field, 190, 1, 166. doi:10.1088/0067-0049/190/1/166
- Jeon, Y., Im, M., Kang, E., et al. 2014, *ApJS*, J- and H-band Imaging of AKARI North Ecliptic Pole Survey Field, 214, 2, 20. doi:10.1088/0067-0049/214/2/20
- Kaspi, S., Maoz, D., Netzer, H., et al. 2005, *ApJ*, The Relationship between Luminosity and Broad-Line Region Size in Active Galactic Nuclei, 629, 1, 61. doi:10.1086/431275
- Kim, D., Im, M., & Kim, M. 2010, *ApJ*, New Estimators of Black Hole Mass in Active Galactic Nuclei with Hydrogen Paschen Lines, 724, 1, 386. doi:10.1088/0004-637X/724/1/386
- Kim, S. J., Lee, H. M., Matsuhara, H., et al. 2012, *A&A*, The North Ecliptic Pole Wide survey of AKARI: a near- and mid-infrared source catalog, 548, A29. doi:10.1051/0004-6361/201219105
- Kim, D., Im, M., Glikman, E., et al. 2015, *ApJ*, Accretion Rates of Red Quasars from the Hydrogen P $\beta$  Line, 812, 1, 66. doi:10.1088/0004-637X/812/1/66
- Kim, D., Im, M., Kim, J. H., et al. 2015, *ApJS*, The AKARI 2.5-5.0  $\mu$ m Spectral Atlas of Type-1 Active Galactic Nuclei: Black Hole Mass Estimator, Line Ratio, and Hot Dust Temperature, 216, 1, 17. doi:10.1088/0067-0049/216/1/17
- Kim, D. & Im, M. 2018, *A&A*, What makes red quasars red?. Observational evidence for dust extinction from line ratio analysis, 610, A31. doi:10.1051/0004-6361/201731963
- Kim, D., Im, M., Canalizo, G., et al. 2018, *ApJS*, 238, 2, 37. doi:10.3847/1538-4365/aadfd5
- Kim, D., Im, M., Kim, M., et al. 2020, *ApJ*, Gemini Multi-Object Spectrograph Integral Field Unit Spectroscopy of the Double-peaked Broad Emission Line of a Red Active Galactic Nucleus, 894, 2, 126. doi:10.3847/1538-4357/ab86a4
- Kim, S. J., Oi, N., Goto, T., et al. 2021, *MNRAS*, Identification of AKARI infrared sources by the Deep HSC Optical Survey: construction of a new band-merged catalogue in the North Ecliptic Pole Wide field, 500, 3, 4078. doi:10.1093/mnras/staa3359
- Kim, D., Lee, D., & Im, M. 2022, *MNRAS*, Bolometric luminosity estimators using infrared hydrogen lines for dust obscured active galactic nuclei, 509, 1, 1147. doi:10.1093/mnras/stab3072
- Kim, D., Im, M., Kim, M., et al. 2023, *ApJ*, Estimators of Bolometric Luminosity and Black Hole Mass with Mid-infrared Continuum Luminosities for Dust-obscured Quasars: Prevalence of Dust-obscured SDSS Quasars, 954, 2, 156. doi:10.3847/1538-4357/aceb5e
- Kim, D., Im, M., Lim, G., et al. 2024, *Journal of Korean Astronomical Society*, Eddington Ratios of Dust-Obscured Quasars at  $z \sim 2$ , 57, 95. doi:10.5303/JKAS.2024.57.1.95
- Kim, D., Kim, Y., Im, M., et al. 2024, *A&A*, Eddington ratios of dust-obscured quasars at  $z \lesssim 1$ : Evidence supporting dust-obscured quasars as young quasars, 690, A283. doi:10.1051/0004-6361/202450290
- Kim, M., Son, S., & Ho, L. C. 2024, *A&A*, 689, A27. doi:10.1051/0004-6361/202450413
- Kim, Y., Kim, D., Im, M., et al. 2024, *ApJ*, 972, 2, 171. doi:10.3847/1538-4357/ad5d5d
- Kim, D. & Im, M. 2025, *ApJ*, JWST Spectroscopic View of a Rapidly Growing, Dust-obscured Quasar at  $z \sim 4$ : Effect of Dust Extinction Correction on Black Hole Mass and Eddington Ratio Estimation, 983, 1, 55. doi:10.3847/1538-4357/adbd44
- Kocevski, D. D., Brightman, M., Nandra, K., et al. 2015, *ApJ*, 814, 2, 104. doi:10.1088/0004-637X/814/2/104
- Krawczyk, C. M., Richards, G. T., Mehta, S. S., et al. 2013, *ApJS*, 206, 1, 4. doi:10.1088/0067-0049/206/1/4
- Krumpe, M., Miyaji, T., Brunner, H., et al. 2015, *MNRAS*, 446, 1, 911. doi:10.1093/mnras/stu2010
- La Franca, F., Onori, F., Ricci, F., et al. 2015, *MNRAS*, 449, 2, 1526. doi:10.1093/mnras/stv368
- La Marca, A., Margalef-Bentabol, B., Wang, L., et al. 2024, *A&A*, 690, A326. doi:10.1051/0004-6361/202348188
- Landt, H., Ward, M. J., Peterson, B. M., et al. 2013, *MNRAS*, 432, 1, 113. doi:10.1093/mnras/stt421
- Lee, H. M., Kim, S. J., Im, M., et al. 2009, *PASJ*, North Ecliptic Pole Wide Field Survey of AKARI: Survey Strategy and Data Characteristics, 61, 375. doi:10.1093/pasj/61.2.375
- Malkan, M. A. 1983, *ApJ*, 268, 582. doi:10.1086/160981

- Markwardt, C. B. 2009, *Astronomical Data Analysis Software and Systems XVIII*, 411, 251. doi:10.48550/arXiv.0902.2850
- Martin, D. C., Fanson, J., Schiminovich, D., et al. 2005, *ApJL*, The Galaxy Evolution Explorer: A Space Ultraviolet Survey Mission, 619, 1, L1. doi:10.1086/426387
- Martínez-Sansigre, A., Rawlings, S., Lacy, M., et al. 2005, *Nature*, 436, 7051, 666. doi:10.1038/nature03829
- Matsuhara, H., Wada, T., Matsuura, S., et al. 2006, *PASJ*, Deep Extragalactic Surveys around the Ecliptic Poles with AKARI (ASTRO-F), 58, 673. doi:10.1093/pasj/58.4.673
- McLure, R. J. & Dunlop, J. S. 2004, *MNRAS*, The cosmological evolution of quasar black hole masses, 352, 4, 1390. doi:10.1111/j.1365-2966.2004.08034.x
- Merloni, A., Predehl, P., Becker, W., et al. 2012, *eROSITA Science Book: Mapping the Structure of the Energetic Universe*, arXiv:1209.3114. doi:10.48550/arXiv.1209.3114
- Mezcua, M., Prieto, M. A., Fernández-Ontiveros, J. A., et al. 2016, *MNRAS*, 457, 1, L94. doi:10.1093/mnras/1slv209
- Miyazaki, S., Komiya, Y., Kawanomoto, S., et al. 2018, *PASJ*, Hyper Suprime-Cam: System design and verification of image quality, 70, S1. doi:10.1093/pasj/psx063
- Murakami, H., Baba, H., Barthel, P., et al. 2007, *PASJ*, The Infrared Astronomical Mission AKARI\*, 59, S369. doi:10.1093/pasj/59.sp2.S369
- Nayeri, H., Ghotbi, N., Cooray, A., et al. 2018, *ApJS*, Spitzer Observations of the North Ecliptic Pole, 234, 2, 38. doi:10.3847/1538-4365/aaa07e
- Oi, N., Goto, T., Matsuhara, H., et al. 2021, *MNRAS*, Subaru/HSC deep optical imaging of infrared sources in the AKARI North Ecliptic Pole-Wide field, 500, 4, 5024. doi:10.1093/mnras/staa3080
- Onaka, T., Matsuhara, H., Wada, T., et al. 2007, *PASJ*, The Infrared Camera (IRC) for AKARI – Design and Imaging Performance, 59, S401. doi:10.1093/pasj/59.sp2.S401
- Páris, I., Petitjean, P., Aubourg, É., et al. 2018, *A&A*, 613, A51. doi:10.1051/0004-6361/201732445
- Polletta, M., Weedman, D., Hönic, S., et al. 2008, *ApJ*, 675, 2, 960. doi:10.1086/524343
- Pearson, C., Cheale, R., Serjeant, S., et al. 2017, *Publication of Korean Astronomical Society*, 32, 1, 219. doi:10.5303/PKAS.2017.32.1.219
- Pearson, C., Barrufet, L., Campos Varillas, M. del C., et al. 2019, *PASJ*, The Herschel-PACS North Ecliptic Pole Survey, 71, 1, 13. doi:10.1093/pasj/psy107
- Peca, A., Cappelluti, N., Urry, C. M., et al. 2023, *ApJ*, 943, 2, 162. doi:10.3847/1538-4357/acac28
- Peterson, B. M., Ferrarese, L., Gilbert, K. M., et al. 2004, *ApJ*, Central Masses and Broad-Line Region Sizes of Active Galactic Nuclei. II. A Homogeneous Analysis of a Large Reverberation-Mapping Database, 613, 2, 682. doi:10.1086/423269
- Pilbratt, G. L., Riedinger, J. R., Passvogel, T., et al. 2010, *A&A*, Herschel Space Observatory. An ESA facility for far-infrared and submillimetre astronomy, 518, L1. doi:10.1051/0004-6361/201014759
- Planck Collaboration, Ade, P. A. R., Aghanim, N., et al. 2016, *A&A*, Planck 2015 results. XIII. Cosmological parameters, 594, A13. doi:10.1051/0004-6361/201525830
- Predehl, P., Andritschke, R., Arefiev, V., et al. 2021, *A&A*, 647, A1. doi:10.1051/0004-6361/202039313
- Rakshit, S., Stalin, C. S., & Kotilainen, J. 2020, *ApJS*, 249, 1, 17. doi:10.3847/1538-4365/ab99c5
- Ren, W., Guo, H., Shen, Y., et al. 2024, *ApJ*, 974, 2, 153. doi:10.3847/1538-4357/ad6e76
- Ricci, F., La Franca, F., Onori, F., et al. 2017, *A&A*, 598, A51. doi:10.1051/0004-6361/201629380
- Richards, G. T., Lacy, M., Storrie-Lombardi, L. J., et al. 2006, *ApJS*, 166, 2, 470. doi:10.1086/506525
- Rose, M., Tadhunter, C. N., Holt, J., et al. 2013, *MNRAS*, 432, 3, 2150. doi:10.1093/mnras/stt564
- Runnoe, J. C., Brotherton, M. S., & Shang, Z. 2012, *MNRAS*, 422, 1, 478. doi:10.1111/j.1365-2966.2012.20620.x
- Schlafly, E. F. & Finkbeiner, D. P. 2011, *ApJ*, 737, 2, 103. doi:10.1088/0004-637X/737/2/103
- Schlegel, D. J., Finkbeiner, D. P., & Davis, M. 1998, *ApJ*, 500, 2, 525. doi:10.1086/305772
- Scott, J. E., Kriss, G. A., Brotherton, M., et al. 2004, *ApJ*, 615, 1, 135. doi:10.1086/422336
- Shen, Y., Richards, G. T., Strauss, M. A., et al. 2011, *ApJS*, A Catalog of Quasar Properties from Sloan Digital Sky Survey Data Release 7, 194, 2, 45. doi:10.1088/0067-0049/194/2/45
- Shen, Y., Hall, P. B., Horne, K., et al. 2019, *ApJS*, 241, 2, 34. doi:10.3847/1538-4365/ab074f
- Shim, H., Im, M., Ko, J., et al. 2013, *ApJS*, Hectospec and Hydra Spectra of Infrared Luminous Sources in the AKARI North Ecliptic Pole Survey Field, 207, 2, 37. doi:10.1088/0067-0049/207/2/37
- Shim, H., Kim, Y., Lee, D., et al. 2020, *MNRAS*, NEPSC2, the North Ecliptic Pole SCUBA-2 survey: 850- $\mu\text{m}$  map and catalogue of 850- $\mu\text{m}$ -selected sources over 2 deg<sup>2</sup>, 498, 4, 5065. doi:10.1093/mnras/staa2621

- Singha, M., Husemann, B., Urrutia, T., et al. 2022, *A&A*, 659, A123. doi:10.1051/0004-6361/202040122
- Son, S., Kim, M., & Ho, L. C. 2023, *ApJ*, 953, 2, 175. doi:10.3847/1538-4357/ace165
- Suh, H., Civano, F., Hasinger, G., et al. 2019, *ApJ*, 872, 2, 168. doi:10.3847/1538-4357/ab01fb
- Toba, Y., Oyabu, S., Matsuhara, H., et al. 2013, *PASJ*, 65, 113. doi:10.1093/pasj/65.5.113
- Toba, Y., Goto, T., Oi, N., et al. 2020, *ApJ*, 899, 1, 35. doi:10.3847/1538-4357/ab9cb7
- Truemper, J. 1982, *Advances in Space Research, The ROSAT mission*, 2, 4, 241. doi:10.1016/0273-1177(82)90070-9
- Urrutia, T., Lacy, M., Spoon, H., et al. 2012, *ApJ*, 757, 2, 125. doi:10.1088/0004-637X/757/2/125
- Urry, C. M. & Padovani, P. 1995, *PASP*, 107, 803. doi:10.1086/133630
- Virtanen, P., Gommers, R., Oliphant, T. E., et al. 2020, *Nature Medicine*, 17, 261. doi:10.1038/s41592-019-0686-2
- Weingartner, J. C. & Draine, B. T. 2001, *ApJ*, 548, 1, 296. doi:10.1086/318651
- Werner, M. W., Roellig, T. L., Low, F. J., et al. 2004, *ApJS, The Spitzer Space Telescope Mission*, 154, 1, 1. doi:10.1086/422992
- White, G. J., Pearson, C., Braun, R., et al. 2010, *A&A, A deep survey of the AKARI north ecliptic pole field . I. WSRT 20 cm radio survey description, observations and data reduction*, 517, A54. doi:10.1051/0004-6361/200913366
- Wilkes, B. J., Schmidt, G. D., Cutri, R. M., et al. 2002, *ApJL*, 564, 2, L65. doi:10.1086/338908
- Wright, E. L., Eisenhardt, P. R. M., Mainzer, A. K., et al. 2010, *AJ, The Wide-field Infrared Survey Explorer (WISE): Mission Description and Initial On-orbit Performance*, 140, 6, 1868. doi:10.1088/0004-6256/140/6/1868
- Xu, D., Komossa, S., Zhou, H., et al. 2007, *ApJ*, 670, 1, 60. doi:10.1086/521697
- Zhou, H., Wang, T., Yuan, W., et al. 2006, *ApJS*, 166, 1, 128. doi:10.1086/504869